Somatostatin peptide signaling dampens cortical circuits and promotes exploratory behavior

Dakota F. Brockway[1,2], J. Brody Moyer[2], Chloe M. Aloimonos[3], Thomas Clarity[3], Keith R. Griffith[2,4], Grace C. Smith[2,4], Nigel C. Dao[2], Md Shakhawat Hossain[4], Patrick J. Drew[1,2,4,5,6], Joshua A. Gordon[3,7], David A. Kupferschmidt[3], Nicole A. Crowley[1,2,4,5]

Affiliations:

[1]Neuroscience Graduate program, Huck Institute of the Life Sciences, The Pennsylvania State University

[2]Department of Biology, The Pennsylvania State University

[3]Integrative Neuroscience Section, National Institute of Neurological Disorders and Stroke, National Institutes of Health

[4]Department of Biomedical Engineering, The Pennsylvania State University

[5]Center for Neural Engineering, The Pennsylvania State University

[6]Departments of Engineering Science and Mechanics and Neurosurgery, The Pennsylvania State University

[7]Office of the Director, National Institute of Mental Health, National Institutes of Health

Corresponding Author:
Nicole A. Crowley, Ph.D.
326 Mueller Lab
Penn State University
University Park, PA 16802
nzc27@psu.edu

Keywords:
Somatostatin, anxiety, prelimbic cortex, peptides

Running Title:
Somatostatin in the prelimbic cortex

ABSTRACT

Background Somatostatin (SST) neurons in the prelimbic (PL) cortex mediate a variety of behavioral states, ranging from alcohol consumption to fear learning and avoidance-related behaviors. However, little is known about the role of somatostatin peptide signaling itself to cortical functioning and behavior. Here, we sought to characterize the unique physiological and behavioral roles of the SST peptide in the PL cortex.

Methods We employed a combination of *ex vivo* electrophysiology, *in vivo* calcium monitoring, and *in vivo* peptide pharmacology to explore the role of SST neuron and peptide signaling in the mouse PL cortex. Whole-cell slice electrophysiology was conducted in C57BL/6J male and female mice in pyramidal and GABAergic neurons of the PL cortex to characterize the pharmacological mechanism of SST signaling. Fiber photometry recordings of GCaMP6f fluorescent calcium signals from SST neurons were conducted to characterize the activity profile of SST neurons during exploration of an elevated plus maze (EPM) and open field (OF). We further used local delivery of a broad SST receptor (SSTR) agonist into bilateral PL cortex to test causal effects of SST signaling on these same exploratory behaviors.

Results SSTR activation broadly hyperpolarized layer 2/3 pyramidal neurons in the PL cortex in both male and female mice *ex vivo*, through both monosynaptic and polysynaptic GABA neuron-mediated mechanisms of action. This hyperpolarization was blocked by pre-application of the SSTR antagonist cyclo-somatostatin (cyclo-SST) and was non-reversible. SST neurons in PL were activated during EPM and OF exploration, indicating task-related recruitment of these neurons. Lastly, in line with this exploration-related activity profile, SSTR agonist administration directly into the PL enhanced open arm exploration in the EPM.

Conclusions Here we reveal a novel role for the SST peptide system within the PL cortex, by demonstrating a peptide-induced hypoexcitability of PL circuits and modulation of PL-dependent exploratory behaviors.

INTRODUCTION

The prefrontal cortex contains a complex microcircuitry of γ-Aminobutyric acid (GABA)-expressing inhibitory neurons capable of modulating excitatory cortical outputs involved in a range of behaviors. Somatostatin (SST) neurons within the prelimbic (PL) cortex have been implicated in a variety of neuropsychiatric diseases and associated behavioral states (Brockway and Crowley, 2020; Crowley and Joffe, 2021). SST neurons play a role in binge alcohol drinking (Dao et al., 2021), fear learning (Cummings and Clem, 2020), and the interaction between substance use and avoidance states (Dao et al., 2020). These neurons also facilitate oscillatory synchrony between the prefrontal cortex and the hippocampus (Abbas et al., 2018), an established neural correlate of avoidance behaviors (Adhikari, Topiwala and Gordon, 2010, 2011; Padilla-Coreano *et al.*, 2016, 2019). In addition, SST neurons are active during restraint stress (Joffe et al., 2022), highlighting the rapid activation of SST neurons during behaviors related to stress or threat. However, despite the abundance of this peptidergic neuronal subtype within the PL cortex (Brockway and Crowley, 2020), little is known about how SST itself functions as a signaling molecule in this region, and what role this peptide plays in modulating behavior. Traditionally, it has proven difficult to separate GABAergic from peptidergic transmission due to technological barriers in probing these signaling molecules separately. Understanding the potential differing roles of GABA and SST is vital for understanding the unique contributions of SST to neuronal modulation, as well as for uncovering its potential as a therapeutic target.

Neuropeptides including SST are thought to be stored in dense core vesicles (Merighi, 2018), and can often diffuse greater distances than traditional neurotransmitters. They exert long lasting effects by activating G-protein coupled receptor (GPCR) signaling cascades. These properties of neuropeptides position them to modulate neuronal circuits and behaviors in unique and diverse ways (Kash *et al.*, 2015; Brockway and Crowley, 2020). SST signals through five GPCRs which are predominately $G_{i/o}$ coupled and are expressed throughout the mammalian cortex (Patel *et al.*, 1994; Liguz-Lecznar, Urban-Ciecko and Kossut, 2016). The human clinical literature suggests a strong 'pro-resiliency' role for SST. SST mRNA in the prefrontal cortex is decreased in individuals with bipolar disorder (Fung *et al.*, 2014), and similar decreases are seen in post-mortem tissue of those with major depressive disorder (Sibille *et al.*, 2011) and schizophrenia (Hashimoto *et al.*, 2008). Similarly, recent clinical work demonstrated that alcohol-induced changes in local functional connectivity are dependent

on overall SST gene expression in healthy individuals, with greater SST gene expression corresponding to decreased alcohol-induced changes (Ochi *et al.*, 2022). Together, the human literature provides ample evidence for SST as a positive marker for the healthy brain, with decreasing expression, independent of GABAergic changes, associating with a host of neuropsychiatric disorders. While we have previously characterized the activity conditions that promote endogenous release of SST from PL cortical neurons (Dao, Brockway and Crowley, 2019), little work has systematically explored SST's downstream actions. Here, we attempt to bridge the gap between the known effects of GABA signaling arising from SST neurons and the potential actions of SST peptidergic signaling itself.

We demonstrated the role of SST peptide and neuronal signaling in the PL cortex using a three-pronged approach. First, we used slice electrophysiology to demonstrate the physiological actions of SST peptidergic signaling on cortical microcircuits in both male and female mice. Second, we turned to *in vivo* fiber photometry to assess whether these neurons are activated during exploratory behaviors in a manner that might promote endogenous peptide release. Lastly, we directly administered an SSTR agonist into the PL cortex to assess the causal effects of SST signaling on these same exploratory behaviors.

Together, this work demonstrates that SST acts in the PL cortex to hyperpolarize cortical pyramidal neurons, that SST neurons are recruited during exploratory behaviors, and that SSTR activation promotes exploration, suggesting that SST signaling is a promising target for modulating cortical circuits in both sexes.

MATERIALS AND METHODS

Animals

All animal procedures were performed in accordance with the Institutional Animal Care and Use Committees (IACUC) at The Pennsylvania State University and The National Institute on Neurological Disorders and Stroke (NINDS), conforming to US National Institutes of Health guidelines. Adult male and female C57BL/6J mice were bred in house for electrophysiology or ordered from Jackson Labs (strain #000664, Bar Harbor, ME) for cannula experiments. Female and male VIP::Cre;SST::Flp mice (Jackson Labs strain # 010908 and 028579, respectively; heterozygous for both recombinases) were bred in house from crossings of homozygous VIP::Cre;SST::Flp females and Df(16)A$^{+/-}$ males (Stark *et al.*, 2008) for the fiber photometry

experiments. Df(16)A$^{+/-}$ male breeders were backcrossed for more than 10 generations on a C57BL/6J background. All mice used for photometry were wildtype at the Df(16)A locus (i.e., Df(16)A$^{+/+}$). Mice were maintained on a 12-h light cycle (lights on at 7:00 am, vivarium temperature 21°C, ±1°C). All electrophysiology and cannula experiments were conducted at The Pennsylvania State University, and all fiber photometry experiments were conducted at the NINDS.

Electrophysiology

Mice were deeply anesthetized via inhaled isoflurane (5% in oxygen, v/v) and rapidly decapitated. Brains were quickly removed and processed according to the N-methyl-D-glucamine (NMDG) protective recovery method (Ting et al., 2018). Brains were immediately placed in ice-cold oxygenated NMDG-HEPES artificial cerebrospinal fluid (aCSF) containing the following, in mM: 92 NMDG, 2.5 KCl, 1.25 NaH_2PO_4, 30 $NaHCO_3$, 20 HEPES, 25 glucose, 2 thiourea, 5 Na-ascorbate, 3 Na-pyruvate, 0.5 $CaCl_2{\cdot}2H_2O$, and 10 $MgSO_4{\cdot}7H_2O$ (pH to 7.3–7.4). The PL was identified according to the Allen Mouse Brain Atlas. 300 µM coronal slices containing the PL were prepared on a Compresstome Vibrating Microtome VF-300-0Z (Precisionary Instruments, Greenville, NC), and transferred to heated (31°C) NMDG-HEPES (in mM: 124 NaCl, 4.4 KCl, 2 $CaCl_2$, 1.2 $MgSO_4$, 1 NaH_2PO_4, 10.0 glucose, and 26.0 $NaHCO_3$, pH 7.4, mOsm 300-310), for a maximum of 10 min. Slices were then transferred to heated (31°C) oxygenated normal aCSF where they were allowed to rest for at least 1 h before use. Finally, slices were moved to a submerged recording chamber where they were continuously perfused with the recording aCSF (2 mL per min flow rate, 31°C). Recording electrodes (3–6 MΩ) were pulled from thin-walled borosilicate glass capillaries with a Narishige P-100 Puller. Drugs were included in the aCSF as described below per experiment.

Pyramidal and GABAergic neurons in layer 2/3 of the PL cortex were identified by location from midline, morphology (prominent triangular soma and apical dendrites for pyramidal neurons), and membrane characteristics, consistent with previously published electrophysiology in PL cortex layer 2/3 pyramidal neurons (Lowery-Gionta et al., 2018; Cummings and Clem, 2020; Dao et al., 2021). Pyramidal and non-pyramidal neurons were further confirmed by membrane properties and action potential width (Dao et al., 2021).

All experiments used a potassium-gluconate (KGluc)-based intracellular recording solution, containing the following (in mM): 135 K-Gluc, 5 NaCl, 2 MgCl2, 10 HEPES, 0.6 EGTA, 4 Na2ATP, and 0.4 Na2GTP (287–290 mOsm, pH 7.35). Following rupture of the cell membrane, cells were held in current-clamp. A minimum of 5 min stable baseline was acquired prior to experiments and bath application of drugs. Measurements of intrinsic excitability were conducted at both resting membrane potential (RMP) and at the standard holding potential of −70 mV both before and after application of drugs. Gap-free RMP was recorded during the entire drug application period. Measurements of intrinsic excitability included the RMP, rheobase (the minimum amount of current needed to elicit an action potential during a current ramp protocol), action potential threshold (the membrane potential at which the first action potential fired during the current ramp), and the number of action potentials fired during a voltage-current plot protocol (VI plot) with increasing steps of depolarizing currents (0–200 pA, 10 pA per step). Hyperpolarizing currents (not shown) were included as a control. Some experiments were conducted in tetrodotoxin (500 nM) as noted to isolate monosynaptic activity. Input resistance was monitored continuously throughout the experiment, and when it deviated by more than 20% the experiment was discarded.

Stereotaxic surgeries for cannula implantation

Custom bilateral cannulas targeted at the PL cortex were purchased from P1 Technologies (Roanoke, VA). Mice were deeply anesthetized with isoflurane (5% induction, 1-2% maintenance) and mounted on a stereotaxic frame (Stoelting, Wood Dale, IL). Following craniotomy, drill holes were targeted at the PL cortex (from Bregma: AP +1.8 mm, ML +/- 0.5 mm). Two additional drill holes were placed posterior to the injection site for bone screws. The guide cannula was lowered to the injection site for a final depth of -1.67 mm. Dental cement was used to secure the guide cannula, a dummy cannula was inserted, and Vetbond used for any additional scalp closure. Mice were allowed to recover for a minimum of one week prior to behavioral testing. Placements of cannulas for all mice were verified by histology at the conclusion of the experiments.

Stereotaxic surgeries for fiber photometry

Adeno-associated virus (AAV) encoding Flp-dependent GCaMP6f (AAV9.Ef1a.fDIO.GCaMP6f) was packaged by Vector Biolabs using a plasmid from Addgene (#118273). AAV encoding Cre-dependent TdTomato (AAV9.CAG.FLEX.TdTomato) was purchased from Addgene (#51503). Titers of the GCaMP6f and TdTomato viruses were $1x10^{12}$ and $1.9x10^{13}$ GC/mL, respectively, and were combined 10:1 (GCaMP:TdTomato) immediately prior to injection. All stereotaxic viral injections were conducted using aseptic surgical technique. Mice aged 12-16 weeks were deeply anesthetized with 5% isoflurane in oxygen (v/v) and secured in a stereotaxic frame (Kopf Instruments, Germany). Sedation was maintained using 1%–2% isoflurane during surgery. A midline incision was made on the scalp and two miniature screws (Antrin Miniature Specialities, Inc.) were secured to the skull. A craniotomy was performed above the left PL cortex according to the coordinates (in mm) +1.95 A/P (from bregma), -0.4 M/L (from bregma), -1.5 (from dura). The combined viruses were microinjected from pulled glass capillaries (using PC-100, Narishige) using a syringe (#7634-01, Hamilton) and syringe pump (#53311, Stoelting) with a volume of 500 nL and a rate of 100 nL/min. After infusion, the needle was left in place for 10 min to allow the virus to diffuse before the needle was slowly withdrawn. A fiber optic cannula (200μm core, 0.39 NA; CFMC12L05, ThorLabs) was implanted into the same craniotomy, with the coordinates (in mm) +1.95 A/P (from bregma), -0.4 M/L (from bregma), -1.0 (from dura). Dental cement (Unifast Trad) was used to adhere the ferrule/fiber to the skull. Tissue was secured to the dental cement with VetBond adhesive (1469Sb, 3M). Following surgery, mice were returned to group housing for 5-7 weeks prior to behavioral testing and photometric recording.

In vivo fiber photometry apparatus

A custom-built spectrometer-based system was used to conduct fiber photometry recordings. Blue light from a 473-nm laser (MBL-III-473-100mW, Ready Lasers) was directed through a Noise Eater (NEL01, ThorLabs) and into a kinematic fluorescence filter cube (DFM1, ThorLabs) onto a dual-edge dichroic mirror (ZT488/561rpc, Chroma). Light was then coupled using a FC/PC fiber coupler (PAF2-A4A, ThorLabs) into a fiber patchcord (M72L05, 200um core, 0.39 NA, ThorLabs) connected to a fiberoptic rotary joint (FRJ_1x1_FC-FC, Doric Lenses) followed by another patchcord (200-um core, 0.39 NA, Doric). Blue light power was approximately 80 μW at the ferrule end of the final patchcord, resulting in ~70 μW output from the surgically

implanted ferrule. On each recording day, the surgically implanted ferrule was cleaned with 70% ethanol and lens paper (806, Ted Pella) and securely attached to the ferrule end of the final patchchord via a mating sleeve (SM-CS1140S, Precision Fiber Products). Fluorescence emission from the tissue was collected by the same fiber, filtered through a dual-band emission filter (ZET488/561m, Chroma), and directed using a fiber coupler (PAF2S-11A, Thorlabs) into a 200-µm core, anti-reflection-coated fiber (M200L02S-A, ThorLabs) which was led to a spectrometer (Ocean Insight, QEPro). The spectrometer quantified photon counts across a ~350-1130 nm wavelength window. Spectra comprised of integrated photons captured over a 37-ms time window were sampled at a frequency of 20 Hz.

Drugs

For behavior, Octreotide Acetate (Sigma Aldrich, PHR 1880) was dissolved in sterile aCSF at 327 µM, aliquoted at 100 µL, stored at −20 C, and diluted as needed. For electrophysiology, Octreotide Acetate was dissolved in ddH2O at 1 mM, aliquoted at 100 µL, stored at -20 C, and diluted as needed. SST (Bachem, H-1490) was dissolved in ddH2O at 1 mM, aliquoted at 50 µL, stored at −20 C, and diluted to 1 µM in aCSF as needed. Cyclosomatostatin (cyclo-SST; Abcam, ab141211) was dissolved in DMSO at 1 mM, aliquoted at 100 µL, stored at −20 C, and diluted to 1 µM in aCSF as needed. Tetrodotoxin (TTX) (Abcam, ab120054) was dissolved in ddH2O at 5 mM, aliquoted at 50 µL, stored at −20 C, and diluted to 500 nM in aCSF as needed.

Drug microinjection procedure

Drug microinjection protocols were adapted from previously published studies (Sajadi et al., 2016). Mice were habituated to handling and manipulation of the dummy cannula for 3 consecutive days prior to behavioral testing. Octreotide or aCSF control was injected at an infusion rate of 0.1 µL/min over 3 minutes. Due to limited literature on *in vivo* targeting of SSTRs, we initially piloted a broad dose-response curve (**Supplemental Figure 5**); in these pilot experiments, mice were randomized to one of 4 octreotide groups - 0.00 ug (aCSF control), 0.001 µg, 0.01 µg or 0.1 µg / 300 nL / hemisphere. The infusion cannula was left in place for 2 min to allow for efficient diffusion of the injected solution. Subsequent behavior was conducted with 0.001 µg / 300nL per hemisphere.

Behavior

Identical open field test (OFT) and elevated plus maze (EPM) arenas were constructed at The Pennsylvania State University and NINDS. Behavioral experiments were done during the light cycle and mice were brought to the testing room and allowed to rest for at least 1 h prior to experimentation. Behavioral tests were separated by 48 hrs and their order was counterbalanced across mice.

For the OFT, mice were initially placed in the corner of a 50 x 50 x 20 cm arena and allowed to explore for 30 min. The total distance traveled over 30 min and the time spent in the 30 x 30 cm center square were quantified.

For the EPM test, mice were placed into the center square of an elevated (40 cm) crossbar with two open and two closed arms (30 x 5 cm), facing a closed arm (20 cm walls of Plexiglas). Mice were allowed to explore the maze for 5 min (drug cannula experiments) and 10 min (fiber photometry) and behavior was video recorded. Mice that fell off the EPM were excluded from the analysis (2 mice total). Percent time spent in the open arms and the percent of entries (open arm entries/total entries x 100) into the open arms were analyzed.

Behavior with fiber photometry

Behavioral testing with photometry recordings was conducted as described above. Mice were first habituated to being handled and tethered to an optical fiber in a bucket for two daily 1-h periods prior to the first OFT/EPM test day. Each test day began with 10 min of blue light administration (~70 μW) in the homecage to stabilize basal GCaMP6f fluorescence and further habituate each mouse to being tethered. A Python-controlled waveform generator (PulsePal v2, SanWorks was used to simultaneously deliver 20-Hz TTLs to the spectrometer (to trigger spectral integration events) and camera (to trigger the camera shutter). Video frames generated at 20Hz were processed in Bonsai operating real-time DeepLabCut processing nodes (Lopes *et al.*, 2015; Kane *et al.*, 2020), such that each frame was assigned coordinates for the maze and mouse as it was captured. Camera shutter events (also 20Hz) were simultaneously captured as digital events in OpenEphys to facilitate subsequent alignment of photometry and positional data (see Behavior Data Analysis).

Photometry/position data were recorded for 10 min during homecage behavior and throughout the subsequent EPM/OFT test. Recordings in both homecage and OFT/EPM were conducted in 2.5-min bins separated by 2 sec. These 2-sec gaps enabled brief openings of a Python-controlled clamp on the fiber optic rotary joint. The clamp prevented light artifacts due to rotary joint movement during recordings. These brief openings allowed for any accumulated patchcord tension to be released prior to reclamping and resumed recording.

Histology for cannula/fiber optic placements and viral expression

Mice were deeply anesthetized with Avertin (250 mg/kg) or isoflurane (5%) and underwent transcardial perfusion, first with ice-cold phosphate buffered saline (PBS) followed by 4% (w/v) paraformaldehyde (PFA). Following perfusion, brains were post-fixed in PFA for 24 h, transferred to PBS and sectioned at 40 µm using a Leica vibratome (VS 1200, Leica) or at 50 µm using a Campden Instruments vibratome (7000 smz2). Sections were mounted on SuperFrost or Marienfeld UniMark glass slides, air dried, and then cover-slipped with Immu-Mount (Thermo Fisher Scientific, Waltham, MA, United States) or DAPI Fluoromount-G (Southern Biotech) mounting media. Slides were then imaged on an Olympus BX63 upright microscope (Center Valley, PA) or a Leica customized epifluorescence scope fitted with a CMS GmbH CMOS camera (Leica Microsystems). The image of representative fiber optic placement and viral expression was captured using a Zeiss LSM 800 confocal microscope. Areas containing the most damage were considered the central location of guide cannula or fiber optic placement. Damage location was then determined in reference to Allen Mouse Brain Atlas and a 0.5 mm projection was added to the end of the damage to account for the internal cannula projection. Mice with cannula/fiber placement outside of the PL cortex were excluded from behavioral/photometry data analysis. 2 of 70 mice for cannula experiments, and 1 of 12 mice for fiber photometry, were removed for misplaced implants.

Behavior data analysis

Behavior for both cannula drug administration and fiber photometry were tracked with DeepLabCut (Mathis *et al.*, 2018). Analysis of cannula drug administration assays was performed in MATLAB; analysis of photometry experiments was performed in Python. Experimenters were blinded to drug injection group throughout the behavioral testing and data analysis.

Microinfusion behavioral analysis

Behavior for cannula drug administration was tracked with DeepLabCut (DLC; Version 2.2.1) and analyzed with custom MATLAB algorithms. For OFT and EPM, three body positions were tracked for behavior classification: the head, middle of the body (caudal to the shoulder joint), and the trunk of the tail. Behavioral recordings that consisted of separate zones included additional tracked points bounding zones of interest. For OFT, these 16 points created boundaries that outlined the edge of the arena (1 point per corner of the 50 cm x 50 cm arena), the center zone (1 point per corner of the central 30 cm x 30 cm square), and each corner (1 point per corner of the 10 cm x 10 cm corner box in the outer zone). Recordings of EPM behavior included the tracking of 12 distinct points that outlined each arm of the maze. Any points that bounded the corner of two zones were only quantified with 1 distinct point to eliminate any redundancies in analysis. Recording of all cannula drug administration behavior was performed using a camera at a frame rate of 29.97 frames per second. OFT and EPM tracking utilized transfer learning to retrain residual network (resnet101) using 9 mice and 10 mice for each behavior, respectively. Mice used for training were selected from recordings performed on separate days whenever possible. DLC model training was considered adequate when confidence in the position was >95%, with most points achieving a confidence >99%. Tracked position coordinates were exported from DLC as CSV file for MATLAB analysis when appropriate confidence levels and tracking performance were reached.

OFT distance was classified as the Euclidean distance of the middle of the mouse body between subsequent frames. Time was initially quantified by the number of frames a mouse was in a polygon bounded by the corners of the zone of interest. All data were then converted from units of pixels/frames to cm/s using known bounds of the arena and the frame rate of the camera. Percent time in a specific zone was quantified as the total time in the zone divided by the total testing time. Behaviors were binned by minutes where appropriate to account for temporal shifts in drug response. Latency to first entry was classified as the time from test start to the first time the mouse body crossed the boundary into the center zone.

EPM distance was classified as the Euclidean distance of the middle of the mouse body between subsequent frames. Time was initially quantified by the number of frames a mouse was in a polygon bounded by the corners of the zone of interest. All data were then converted from units of pixels/frames to cm/s using

known bounds of the arena and the frame rate of the camera. Percent time in a specific zone was quantified as the total time in the zone divided by the total testing time. The central zone connecting arms was classified as a 'dead zone' and not included as a portion of the open or closed arms. Random videos were selected, and behaviors were hand scored where possible to verify both tracking and algorithm accuracy. Experimenters were blinded to injection group throughout the behavioral analysis.

Photometry behavior analysis

Behavioral analysis for the photometry experiments was conducted using many of the same procedures and parameters as described above. In these experiments, Bonsai-DLC was used for behavioral tracking. Bonsai-DLC enabled use of a pre-trained DLC model in a Bonsai workflow to process live-streamed videoframes and generate DLC coordinates in real time. DLC models for the EPM and OFT were created by labelling 300-500 frames per test, comprised of approximately 10-20 frames from each of 20-30 videos of different mice with comparable surgeries/fiber optic tethers to the present experimental mice recorded on different days. In addition to the maze boundaries, six mouse body parts were labelled on each frame: nose, headcap, shoulder, midpoint, hind and basetail. The hind label was used for behavioral analysis. The model was trained for approximately 750,000-1,000,000 iterations, yielding confidence values of >99% in the majority of cases.

A Python-controlled waveform generator (PulsePal v2, SanWorks) delivered 20-Hz TTLs to a FLIR Blackfly S USB3 camera. Each resulting frame was processed for all model-labelled body/maze parts. A confidence threshold of >95% was applied in Bonsai to the positional data. Exported data were down-sampled to 10Hz, and a Kalman Filter (pykalman.github.io) was applied to estimate position data for missing values with confidence <95%. The "opencv homography" Python function was applied to align cohorts with slight variations in camera angles. The hind position from each frame was assigned a maze zone based on the coordinates of the maze boundaries. Brief departures from an assigned zone (e.g., changes from "open_top" > "center" > "open_top") of 3 or less frames were corrected (e.g., converted to all "open_top") to account for noise in the detection around zone boundaries. In the OFT, the timing and number of zone transitions were then calculated based on these assigned zones. In the EPM, because transitions between arms were complicated by the intervening center zone, zone transitions were defined using two sets of criteria. In cases when changes in

assigned zone occurred from one zone to another and back to the original (e.g., "open_top" > "center" > "open_top"), to be assigned a zone transition, the departure (e.g., to "center") needed to last for a minimum of 6 frames. In cases when changes in assigned zone occurred from one zone to another to yet another (e.g., "open_top" > "center" > "closed_left"), to be assigned a zone transition, the departure (e.g., to "center") needed to last for a minimum of 2 frames. These thresholds were implemented to prevent overcounting of re-entries into the same zone, and to accommodate counting of fast transitions between zones (e.g., rapid movement across the center from open to closed arms). Thresholds were determined by cross-referencing DLC-based assignment of transitions with manual assignment by an experimenter in several videos.

Photometry data analysis

The shape and amplitude of the spectrometer-derived fluorescence spectra were used to confirm *in vivo* GCaMP6f and TdTomato expression. Custom Python code was used to calculate the integrated photon count from select 42-nm-wide spectral windows as a measure of GCaMP6f (500-542 nm) and TdTomato (577-619 nm) fluorescence intensity. Integrated photon counts for each color were linear regression-corrected to remove gradual reductions in signal due to fluorophore bleaching across the behavioral test. The ratio of the resulting green and red signals was then calculated (GCaMP:TdTomato; G:T). The G:T timeseries was down-sampled from 20Hz to 10Hz. Z-scores of the G:T ratio were then calculated for each 10-Hz time point, using the mean and standard deviation of their corresponding 2.5-min bin of recorded data. Once aligned to positional data from DeepLabCut, G:T z-scores were then averaged across task relevant periods (e.g., open- vs. closed arms; center vs. surround zones), or aligned to discrete transitions (e.g., center-to-open arms; center-to-surround zones). G:T z-scores were averaged across all events (bouts in an arm/zone, or transitions) within a single animal, and then reported as the average z-score across animals.

Statistics

Experimenters were blinded to groups wherever possible until analysis was completed. Data were analyzed by one-sample t-tests, paired t-tests, 2-way ANOVAs, and post-hoc tests as appropriate and indicated

for each experiment. Statistics and figure preparation were conducted in Prism 9 (GraphPad, La Jolla, CA). Data are expressed as means ± SEM for all figures and considered significant if $p < 0.05$.

RESULTS

Somatostatin has an inhibitory effect on PL cortical circuits

SST hyperpolarizes and decreases excitability of PL cortical pyramidal neurons

To examine the effect of SST on PL cortical circuits, *ex vivo* whole-cell current-clamp recordings were performed on pyramidal neurons in layer 2/3 of the PL cortex in adult male and female C57BL/6J mice (representative circuit diagram in **Figure 1A** for females and **Figure 2A** for males). Males and females were initially analyzed separately. Measurements of intrinsic excitability were conducted at both RMP and at the standard holding potential of −70 mV before and after 10-min bath application of 1 μM SST. Representative traces of rheobase recordings are shown in **Figure 1B** and **Figure 2B** for females and males, respectively, before and after SST application. SST hyperpolarized pyramidal neurons and significantly decreased the RMP in both females ($t_{13} = 2.205$, $p = 0.0460$; **Figure 1C, 1D**) and males ($t_{16} = 2.889$, $p = 0.0107$; **Figure 2C, 2D**). SST also significantly reduced the rheobase in females at both RMP ($t_{13} = 4.916$, $p = 0.0003$) and −70 mV ($t_{13} = 3.953$, $p = 0.0017$; **Figure 1E, 1G**) as well as in males at both RMP ($t_{16} = 4.737$, $p = 0.0002$) and −70 mV ($t_{16} = 2.168$, $p = 0.0456$; **Figure 2E, 2G**). SST significantly increased the action potential threshold at both RMP ($t_{13} = 2.938$, $p = 0.0115$) and −70 mV ($t_{13} = 2.420$, $p = 0.0309$) in females (**Figure 1F, 1H**). However, SST had no effect on action potential threshold at RMP ($t_{16} = 0.5672$, $p = 0.5785$) or −70 mV ($t_{16} = 1.631$, $p = 0.1224$) in males (**Figure 2F, 2H**). Representative traces of VI recordings are shown in **Figure 1I, 1K** and **Figure 2I, 2K** for females and males, respectively. SST significantly reduced the number of action potentials fired in the VI plot at RMP in both females (2-way ANOVA; $F_{current}(20,260) = 18.49$, $p < 0.0001$; $F_{drug}(1,13) = 10.93$, $p = 0.0057$, $F_{current\ x\ drug}(20,260) = 10.98$, $p < 0.0001$; **Figure 1J;** significant post-hoc Bonferroni's are indicated on figures) and males (2-way ANOVA; $F_{current}(20,320) = 14.06$, $p < 0.0001$; $F_{drug}(1,16) = 6.771$, $p = 0.0193$, $F_{current\ x\ drug}(20,320) = 5.600$, $p < 0.0001$; **Figure 2J;** significant post-hoc Bonferroni's are indicated on figures). There was also a significant change in the number of action potentials fired in the VI plot at −70 mV in females (2-way ANOVA; $F_{current}(20,240) = 12.50$, $p < 0.001$; $F_{drug}(1,12) = 1.217$, $p = 0.2916$, $F_{current\ x\ drug}(20,240) = 2.744$, $p < 0.0001$; **Figure**

1L; significant post-hoc Bonferroni's are indicated on figures); however, neither the effect of drug nor drug *x* current interaction were significant in males at −70 mV (2-way ANOVA; $F_{current}(20,320) = 12.63$, p <0.001; $F_{drug}(1,16) = 0.7340$, $p = 0.4043$, $F_{current\ x\ drug}(20,320) = 1.132$, $p = 0.3144$; **Figure 2L**). Because the overall effect of SST on pyramidal neurons was similar in males and females, subsequent electrophysiology experiments combined sexes.

SST actions are blocked, but not reversed, by SSTR antagonists

To confirm that SST is hyperpolarizing pyramidal neurons via canonical SSTR signaling, *ex vivo* whole-cell current-clamp recordings were performed on pyramidal neurons in layer 2/3 of the PL cortex in naïve adult male and female C57BL/6J mice with the addition of 1 μM cyclosomatostatin (cyclo-SST, an SSTR antagonist) in the aCSF prior to and throughout application of SST. When cyclo-SST was present in the aCSF, SST did not significantly alter the RMP (representative circuit diagram in **Supplemental Figure 1A**, rheobase traces in **Supplemental Figure 1B**, bath application in **Supplemental Figure 1C,** and summary RMP in **Supplemental Figure 1D**). SST had no effect on rheobase at RMP (**Supplemental Figure 1E**) or action potential threshold at RMP (**Supplemental Figure 1F**). Further, SST had no effect on the rheobase at −70 mV (**Supplemental Figure 1G**) or action potential threshold at −70 mV (**Supplemental Figure 1H**). Moreover, SST did not affect the number of action potentials fired in the VI plot at either RMP or −70 mV (**Supplemental Fig 1I, 1J**). Together, these experiments confirm that SST-mediated hyperpolarization and reduced excitability of pyramidal neurons is dependent on SSTRs.

To examine whether SST-mediated hyperpolarization and reduced excitability of pyramidal neurons were reversible with post-application of an SSTR antagonist, pyramidal neurons in layer 2/3 of the PL cortex were patched and 1 μM SST applied followed by 1 μM cyclo-SST antagonist application. Results were comparable to those without post-application of the antagonist in **Figures 1-2**. SST with a cyclo-SST washout still significantly hyperpolarized the RMP and rheobase at RMP (representative circuit diagram in **Supplemental Figure 2A**, rheobase traces in **Supplemental Figure 2B**, overall bath application of SST and cyclo-SST washout in **Supplemental Figure 2C**, and overall RMP effect in **Supplemental 2D**). While the rheobase at RMP remained similar to the effects of SST alone (**Supplemental Figure 2E**), the action potential threshold at RMP,

rheobase at −70 mV, and action potential threshold at −70 mV were not significantly changed from pre-SST baseline (**Supplemental Figure 2F-H**) This protocol resulted in no significant change in the number of action potentials fired in the VI plot at both RMP and −70 mV (**Supplemental Figure 2I-2L**). This suggests that overall, the effect of SSTR activation on RMP and rheobase is largely not reversible with an SSTR antagonist.

SST effects are dependent on PL cortex microcircuitry

SST hyperpolarized the majority of pyramidal neurons recorded in the PL cortex (**Figure 3A**, data analyzed from **Figures 1B and 2B**). However, a meaningful subset (approximately 35%) of pyramidal neurons depolarized in response to SST, suggesting that the response to SST may depend on the microcircuit with which that pyramidal neuron interacts. To determine whether the hyperpolarizing effects of SST are dependent on polysynaptic activity, we blocked action potentials using 500 nM TTX to isolate monosynaptic connections (representative circuit diagram in **Figure 3B**). When polysynaptic network activity was blocked, all neurons hyperpolarized in response to SST. SST significantly hyperpolarized pyramidal neurons in both males ($t_6 = 5.095$, $p = 0.0022$) and females ($t_4 = 3.448$, $p = 0.0261$; **Figure 3C** overall effect separated by sex). SST significantly decreased the overall RMP ($t_{11} = 0.0715$, $p = 0.0004$; **Figure 3D** sexes combined). This suggests that SST effects on pyramidal neurons are strongest when isolated from polysynaptic circuits, and that the depolarization seen in a subset of pyramidal neurons is driven by their disinhibition by SST actions on neighboring GABAergic neurons.

SST hyperpolarizes and decreases excitability of PL cortical GABAergic neurons

Based on the proposed polysynaptic effect shown in **Figure 3**, *ex vivo* whole-cell current clamp recordings (identical to **Figure 1-3**) were conducted in non-pyramidal, GABAergic populations in the PL cortex (representative circuit diagram in **Figure 4A,** distinguished by morphology, membrane, and electrophysiological properties as outlined above). Representative traces of rheobase recordings before and after SST application are shown in **Figure 4B**. SST hyperpolarized non-pyramidal neurons and significantly decreased the RMP ($t_9 = 2.291$, $p = 0.0477$; **Figure 4C-D**). SST did not significantly alter the rheobase at RMP ($t_9 = 2.046$, $p = 0.0711$; **Figure 4E**), action potential threshold at RMP ($t_9 = 1.751$, $p = 0.1138$; **Figure 4F**),

rheobase at −70 mV (t_9 = 1.320, p = 0.2195; **Figure 4G**), or action potential threshold at −70 mV (t_9 = 1.840, p = 0.0990; **Figure 4H**). However, SST significantly reduced the number of action potentials fired in response to increasing current injection at RMP (2-way ANOVA; $F_{current}(20,180)$ = 22.72, p <0.0001; $F_{drug}(1,9)$ = 6.198, p = 0.344, $F_{current\ x\ drug}(20,180)$ = 8.437, p <0.0001, **Figure 4I-J;** significant post-hoc Bonferroni's are indicated on figure) but not at −70 mV (2-way ANOVA; $F_{current}(20,180)$ = 14, p <0.0001; $F_{drug}(1,9)$ = 0.0183, p = 0.8951, $F_{current\ x\ drug}(20,180)$ = 1.0, p = 0.4063; **Figure 4K-L**). This suggests that SST also acts on GABAergic populations within the PL cortex. When direct, network-independent effects were isolated using TTX (500 nM), SST had no significant effect on the RMP of non-pyramidal neurons in males (t_5 = 2.486, p = 0.0554) or females (t_3= 1.542, p=0.554**; Figure 4N overall effect separated by sex)**. However, when sexes were combined, SST significantly decreased RMP (t_9 = 2.668, p = 0.0257; **Figure4O**).

SST neurons display task-relevant activity during exploratory behaviors

Overall behavior

We next explored whether *in vivo* activity of SST neurons was related to behavioral performance in the EPM and OFT. VIP::Cre;SST::Flp mice were injected in PL cortex with dual AAVs encoding a Flp-dependent GCaMP6f and Cre-dependent TdTomato, and implanted with an optical fiber in PL cortex (schematic and representative histology, **Figure 5A-B**; histology from all mice in **Supplemental Figure 3**). A custom-made dual-color spectrometer-based *in vivo* fiber photometry system was used (schematic in **Figure 5C**, sample fluorescence spectrum in **Figure 5D**). No sex differences were detected in the analyzed behavior or photometry signals, so data were pooled by sex (**Figure 5** and **Supplemental Figure 3**; pink dots denote females, purple dots denote males).

Elevated Plus Maze

SST neurons showed task-related increases in calcium (Ca^{2+}) activity in the EPM (representative heat map of PL SST neuron Ca^{2+} dynamics as a function of location in the EPM in **Figure 5E**, sample photometric recording of GCaMP6f:TdTomato, indicated as G:T, fluorescence during EPM exploration in **Figure 5F;** grey bars denote periods of open arm exploration). On average, SST neuron activity was higher in the open versus

closed arms (t_{10} = 6.101 p < 0.001; **Figure 5G**). In addition, SST neuron activity was dynamically altered around arm transitions in the EPM. SST neuron activity was generally elevated in the six seconds around both transitions from the center of the maze to the open arms, and from the center to the closed arms (**Figure 5H**; left panel shows averages across mice; right panel shows 1-sec bins around transitions; one-sample t-tests vs. 0: center>open: t_{10} = 4.185, p = 0.0019; center>closed: t_{10} = 3,653, p = 0.0044). Whereas SST neuron activity was largely consistent across transitions from the center to the open arms, activity peaked in the two seconds following transitions from the center to the closed arms (Bonferroni-corrected post-hoc one-sample t-tests, *: "0 to 1", p = 0.0024; "1 to 2", p = 0.0078). SST neuron activity dynamics also differed significantly between the two transition types (2-way RM ANOVA: $F_{\text{Time x Transition}}(5,100)$ = 5.912, p < 0.0001; significant post-hoc Šidák's tests: "0 to 1, C>C" diff. from "0 to 1, C>O", p = 0.0134; "0 to 1, C>C" diff. from "C>C" at all other 1-sec bins, p < 0.05; "1 to 2, C>C" diff. from "-2 to -1, C>C", p < 0.05). SST neuron activity during closed but not open arm transitions was also closely aligned to mouse speed during the transitions (**Figure 5I**).

Open Field Test

Similar task-relevant activity of SST neurons was seen in the OFT (representative heat map of PL SST Ca^{2+} dynamics as a function of location in the OFT in **Figure 5J**, and sample photometric recording of G:T fluorescence during OFT in **Figure 5K**; grey bars denote periods of center zone exploration). Similar to recordings during the EPM, average SST neuron activity was higher during exploration of the center of the OFT relative to the surround zone (t_{10} = 2.797, p = 0.0189; **Figure 5L**). Further, SST neuron activity was dynamically altered around zone transitions in the OFT. SST neuron activity was generally elevated in the six seconds around both transitions from the surround to the center, and from the center to surround (**Figure 5M**; one-sample t-tests vs. 0: surround>center: t_{10} = 4.961, p = 0.0006; center>surround: t_{10} = 6.195, p = 0.0001). SST neuron activity gradually increased following transitions from the surround to the center zone (Bonferroni-corrected post-hoc one-sample t-tests, *: "1 to 2", p = 0.0018; "2 to 3", p = 0.0006). In contrast, SST neuron activity was particularly pronounced immediately preceding and following transitions from the center to the surround zone (*: "-1 to 0", p = 0.0024; "0 to 1", p = 0.0006; "0 to 1", p = 0.006). SST neuron activity dynamics also differed significantly between the two transition types (2-way RM ANOVA: $F_{\text{Time x Transition}}(5,100)$ = 11.58, p < 0.0001;

significant post-hoc Šidák's tests: "-1 to 0" and "0 to 1, C>S" diff. from corresponding "S>C", $p < 0.05$; "0 to 1, C>S" diff. from "S>C" at all other 1-sec bins, $p < 0.05$; "1 to 2, C>S" diff. from "2 to 3, C>S", $p < 0.0039$; "-1 to 0, C>S" diff. from "-3 to -2" and "-2 to -1, C>S", $p < 0.01$; "1 to 2, S>C" diff. from "-2 to -1" and "-1 to 0, S>C", $p < 0.05$; "2 to 3, S>C" diff. from "-2 to 1", "-1 to 0" and "0 to 1, S>C", $p < 0.05$; **Figure 5M**). In further similarity to the EPM test, SST neuron activity during transitions from the center to surround zones, but not the reverse, aligned to mouse speed during transitions (**Figure 5N**).

Administration of the SSTR agonist Octreotide results in behavioral phenotypes that recapitulate in vivo fiber photometry activity

Overall behavior

To assess causal effects of SST peptide signaling in the PL cortex during these same exploratory behaviors, the SSTR agonist Octreotide or aCSF control was administered directly to the PL cortex 10 minutes prior to the OFT or EPM via bilateral cannulas (histology from all mice in **Supplemental Figure 5A**).

Elevated Plus Maze

Local administration of the SST targeting compound Octreotide (0.001 µg / 300nL / hemisphere) had no effect on total arm entries or percent open arm entries (representative heat maps in **Figure 6A**; 2-way ANOVA; $F_{sex}(1,26) = 0.4680$, $p = 0.5000$; $F_{drug}(1,26) = 0.3289$, $p = 0.5712$, $F_{sex \times drug}(1,26) = 0.5580$, $p = 0.4618$; **Figure 6B,** significant post-hoc Tukey's are indicated on figure;**;** 2-way ANOVA; $F_{sex}(1,26) = 0.06454$, $p = 0.8015$; $F_{drug}(1,26) = 0.2855$, $p = 0.5976$, $F_{sex \times drug}(1,26) = 1.598$, $p = 0.2174$; **Figure 6C,** significant post-hoc Tukey's are indicated on figure). However, there was a significant interaction between drug and sex for percent time in the open arms (2-way ANOVA; $F_{sex}(1,26) = 0.6452$, $p = 0.4291$; $F_{drug}(1,26) = 3.462$, $p = 0.0741$, $F_{sex \times drug}(1,26) = 7.868$, $p = 0.0094$; **Figure 6D,** significant post-hoc Tukey's are indicated on figure), with a significant increase seen only in male mice treated with Octreotide relative to control. Interestingly, Octreotide-treated male mice, but not female mice, also showed a significant increase in the number of head dips over the open arm of the EPM (2-way ANOVA; $F_{sex}(1,26) = 5.917$, $p=0.0222$; $F_{drug}(1,26) = 3.264$, $p = 0.0824$, $F_{sex \times drug}(1,26) = 5.614$, $p = 0.0255$;

Figure 6E; significant post-hoc Tukey's are indicated on figure). This suggests that administration of an SSTR agonist alters exploratory behavior in a novel context in male, but not female, mice.

Open Field Test

Octreotide administered into PL cortex had no effect on the overall distance traveled in the OFT (2-way ANOVA; $F_{sex}(1,28) = 1.054$, $p=0.3134$; $F_{drug}(1,28) = 0.5550$, $p = 0.4625$, $F_{sex\ x\ drug}(1,28) = 1.855$, $p = 0.1840$; representative heat maps in **Figure 6F**; distance traveled in **Figure 6G**), suggesting the changes seen in the EPM were not due to alterations in gross motor behavior. In addition, Octreotide did not alter the percent time in the center in either sex (2-way ANOVA; $F_{sex}(1,28) = 0.4335$, $p=0.5147$; $F_{drug}(1,28) = 2.426$, $p = 0.1306$, $F_{sex\ x\ drug}(1,28) = 0.02013$, $p = 0.8882$; **Figure 6H**). This suggests that the changes in exploratory behavior induced by Octreotide were unique to the EPM and not driven by changes in general ambulatory behavior.

Validation of octreotide in *ex vivo* electrophysiology experiments

To confirm that the SST-like agonist Octreotide has similar *ex vivo* effects to SST, we performed identical whole-cell current clamp experiments to those conducted with SST but using 3.27 μM Octreotide (corresponding to the concentration used for behavior; **Supplemental Figure 4**). Representative traces of rheobase recordings are shown in **Supplemental Figure 4B and 4N** for females and males, respectively. Octreotide had no significant effect on RMP in females **(Supplemental Figure 4D)**; however, in males Octreotide significantly reduced RMP **(Supplemental Figure 4P)**. Octreotide significantly increased the rheobase at RMP in both females **(Supplemental Figure 4E)** and males **(Supplemental Figure 4Q).** Octreotide did not significantly alter the action potential threshold at RMP in females **(Supplemental Figure 4F)**; however, Octreotide did significantly decrease the action potential threshold at RMP in males **(Supplemental figure 4R)**. Octreotide significantly increased the rheobase at –70 mV in females **(Supplemental Figure 4G);** however, there was no significant change in the rheobase at –70 mV in males **(Supplemental Figure 4S).** Octreotide did not significantly change the action potential threshold at –70 mV in females **(Supplemental Figure 4H)** or males **(Supplemental Figure 4T)**. Octreotide significantly decreased the number of action potentials fired in the VI plot at both RMP and –70 mV in both females **(Supplemental Figure 4J, 4L)** and

males **(Supplemental Figure 4V, 4X).** Overall, while small differences between the sexes and between SST and Octreotide were seen, collectively these data confirm that Octreotide has similar effects to SST in hyperpolarizing and reducing the excitability of pyramidal neurons.

DISCUSSION

Here, we provide the first evidence that SST peptide signaling in the PL cortex acts to broadly dampen cortical circuits in both male and female mice (**Figure 1-4**). We found that SST neurons are preferentially activated when mice explore the open arms of the EPM and the central zone of the OFT, and during transitions between these zones (**Figure 5**), suggesting that SST neurons are recruited in task-relevant exploratory behaviors. Importantly, the fiber photometry studies provided a correlative metric of SST neuronal signaling during exploratory behaviors. The pro-exploratory effects of intra-PL SSTR agonist administration (**Figure 6**) aligned with some of the SST neuron activity dynamics recorded with fiber photometry (notably an increase in open arm time in the EPM). These findings support the overall hypothesis that increased SST neuronal activity observed during the fiber photometry experiments could correspond to endogenous peptide signaling during exploratory behaviors. Collectively, these data suggest that SST and SSTR-targeting compounds alter behavior through inhibition of PL pyramidal neuron outputs and support the need for further investigation teasing apart peptidergic and neurotransmitter actions in these circuits and behaviors.

SST signaling dampens PL cortical output circuits

Results from the present study fill a critical gap in the literature by providing the first evidence that SST acts as an independent signaling molecule to regulate PL cortical neurons. This work demonstrates that SST reduces membrane potential and intrinsic excitability of both glutamatergic (pyramidal) projection populations and GABAergic (non-pyramidal) local microcircuit neurons in the PL cortex (**Figures 1-4**). We found that SST in the PL cortex acts to modulate activity of output pyramidal neurons through monosynaptic and polysynaptic mechanisms. While pyramidal neurons broadly hyperpolarized in response to SST (**Figure 1,2**), a subset depolarized (**Figure 3**). We confirmed that this depolarization was due to disinhibition via polysynaptic GABAergic circuits (e.g., decreased inhibitory input). When network activity was blocked, all pyramidal neurons

hyperpolarized in response to SST (**Figure 3**). Further, we found that GABAergic neurons also broadly hyperpolarized in response to SST (**Figure 4**). The effect of SST on a given neuron may therefore depend on the specific microcircuit in which it is embedded. Indeed, an important avenue of future study is to explore potential specificity of SST effects on different pyramidal neuron output pathways. Similarly, it will be critical to assess whether SST-mediated effects differ across genetically distinct populations of GABAergic neurons, and whether unique glutamatergic inputs onto SST neurons (e.g., those arising from the hippocampus, (Abbas *et al.*, 2018)), drive differing peptidergic effects in PL cortex.

Importantly, SST-mediated hyperpolarization was not reversed by a SSTR antagonist (Supplemental Figure 2). This is consistent with experiments in rats suggesting rapid internalization of some subsets of SSTRs (Schreff *et al.*, 2000). In addition, it is consistent with other neuropeptides which are known to have long lasting effects (van den Pol, 2012), and the non-reversable nature of SST action is consistent with the reported actions of other neuropeptides (e.g., Dynorphin; Crowley *et al.*, 2016). It is also possible that SST stays bound to the receptor, preventing the antagonist from binding. Future work will attempt to elucidate the precise mechanism of this non-reversible effect, as it is key to understanding potential therapeutic strategies that involve SSTR agonism.

Studies have indicated an overall inhibitory role for SST-mediated neuromodulation. For example, SST has been shown to hyperpolarize hippocampal pyramidal cells *in vitro* (Pittman and Siggins, 1981). Other studies have shown that SST can inhibit the release of growth hormones from the pituitary, (Pittman and Siggins, 1981; Song, Yoon and Lee, 2021), reduce both glutamate and GABA transmission onto forebrain cholinergic neurons (Momiyama and Zaborszky, 2006), and inhibit GABA transmission in both the thalamus (Leresche *et al.*, 2000) and striatum (Lopez-Huerta *et al.*, 2008). However, SST may also have an excitatory response at higher concentrations (Delfs and Dichter, 1983). SST also reduces excitability in cortical pyramidal neurons in the developing brain (Riedemann and Sutor, 2019). The precise effect of SST likely depends on various factors, such as the particular brain region and cell type probed, the relative expression of SSTRs 1-5, age, and the concentration of SST. Prior to this investigation, no studies of SST action had been conducted in the PL cortex, and none bridged its *ex vivo* pharmacological circuit effects with related *in vivo* neuronal signaling and behavioral effects.

Previous work from our group demonstrated that SST peptide is released in PL cortex when SST neurons are stimulated at 10 Hz (Dao, Brockway and Crowley, 2019), suggesting that changes in SST neuronal firing rates at relatively low frequencies may correspond to alterations in SST release. Recent rodent studies have implicated PL SST neurons as mediators of various behaviors (Liguz-Lecznar, Urban-Ciecko and Kossut, 2016; Urban-Ciecko and Barth, 2016; Robinson and Thiele, 2020). The neuromodulatory role of SST in the PL presented in the current study suggests that these prior studies should be interpreted as having potential effects on both GABAergic and peptidergic mechanisms. Moreover, reductions in the number of SST neurons observed following chronic stress (Girgenti *et al.*, 2019) and changes in GABAergic populations in patients with neuropsychiatric diseases (Brockway and Crowley, 2020) are likely to result in altered SST neuromodulation alongside altered GABAergic function. Such changes in SST modulation may contribute to dysregulation of PL cortical neurons and outputs and, ultimately be causal to some disease-relevant behaviors. Importantly, the rapid emergence of new optical biosensors for peptides including SST (Xiong *et al.*, 2021; Wang *et al.*, 2022) will allow for new *in vivo* investigation of neurotransmitter versus peptide dynamics. These emerging technologies will allow for the decoupling of SST peptide signaling versus co-released GABA (and potentially other peptides as well). Future work will investigate the precise nature of SST versus GABA release, including in different behavioral paradigms, in different microcircuits, and the interactions between SST and output-specific pyramidal populations.

SST neurons are active during exploration of the EPM and OFT, and peptide administration similarly alters behaviors in these assays

Here, we demonstrate that PL SST neurons broadly signal both zone location and transitions in two separate tasks of exploratory behavior (**Figure 5**). Specifically, our photometry recordings reveal that SST neurons are preferentially activated during exploration of the open versus closed arms of the EPM, and the center versus surround zones of the OFT. The general increase in SST neuron activity in the open arms of the EPM corroborates prior work (Lee *et al.*, 2019). Our recordings further reveal that SST neuron activity aligns with discrete transitions, most notably from center-to-closed arms of the EPM and from center-to-surround zones in the OFT. Our causal evidence that SSTR signaling in PL cortex promotes open arm exploration aligns well with the heightened activation of PL SST neurons in the open arms of the maze. This alignment, and our prior reports

of SST release in response to sustained low-frequency SST neuron activity (Dao, Brockway & Crowley, 2019), suggests that SST peptide may be released during more sustained periods of open arm exploration, and serve as a pro-exploration signal, similar to prior suggestions that SST acts as a "pro-resiliency" peptide. In contrast, SST neuron activation that aligns with rapid transitions from the open arms of the maze may reflect activity that preferentially signals through GABAergic transmission over peptidergic modulation. Our future work will test this hypothesized dichotomy by using, among other approaches, *in vivo* recordings of emerging fluorescent SST sensors.

Importantly, while the fiber photometry experiments did not detect any sex-dependent relationship between SST neuron signaling and exploratory behavior, peptide-induced changes in behavior were only identified in male mice. Other studies have suggested behavioral effects of SST following intracerebroventricular infusion (Engin *et al.*, 2008; Engin and Treit, 2009) and intra-septal and intra-amygdalar infusion (Yeung and Treit, 2012). However, critically, these studies were done exclusively in males, and provided little mechanistic insight. Differences observed in males and females may be due to numerous factors, including potential differences in SSTR density and/or relative prevalence of SSTR subtypes (Pichler *et al.*, 2002). For example, SSTR density is higher in the human brain of males compared to females which may account for the observed effect in males but not females (Pichler *et al.*, 2002). SSTR density is also higher in the male rat arcuate nucleus and pituitary (Selmer *et al.*, 2000). While our data did not suggest that higher doses of the SSTR-targeting compound would have greater efficacy in female mice (**Supplemental Figure 5**), future work will explore SSTR subtype expression and density in the PL cortex in male and female mice, and whether biased ligands may provide differing effects.

SST as a future therapeutic target

Peptides in the PL cortex have begun to gain increased attention for their role in neuropsychiatric diseases. Clinically, SST in the PL cortex is known to be downregulated in numerous neuropsychiatric disorders such as schizophrenia, bipolar disorder, and major depressive disorder positioning it as a potential therapeutic target (Brockway and Crowley, 2020). However, little has been done to understand SST as a signaling molecule

and its potential to confer pro-resiliency behaviors. In the present study, we demonstrate a role for SST in modulating the activity of PL cortical pyramidal and GABAergic populations. Further, we show that PL SST neurons are activated during exploratory behavior, and that activating PL SSTRs can promote exploratory behavior. Taken together, this suggests that activation of these neurons during behavioral tasks may correspond to endogenous peptide release. Future work should further probe the viability of SSTR-targeting compounds for models of clinical disorders.

CONCLUSIONS

Taken together, our work solidifies SST peptide as a key neuromodulator in the PL cortex, by demonstrating its capacity to dampen excitatory and inhibitory network activity and promote a fundamental aspect of animal behavior.

ACKNOLWEDGEMENTS AND DISCLOSURES

This work was funded by the National Institutes of Health (R01 AA 209403, R21 AA028088, and P50 AA017823 to NAC; R01NS078168 to PJD) and National Institute of Neurological Disorders and Stroke Intramural Research Program (ZIA NS003168). The content of this article is solely the responsibility of the authors and does not necessarily represent the official views of the NIH.

Conceptualization: DFB and NAC. Methodology: DFB, MSH, PJD, DAK, JAG, and NAC. Investigation: DFB, JBM, CA, TC, KRG, GCS, NCD, MSH. Visualization: DFB, CA, TC, KRG, MSH, DAK, and NAC. Funding acquisition: PJD, DAK, JAG, and NAC. Project administration: PJD, DAK, and NAC. Supervision: PJD, DAK, and NAC. Writing: DFB, PJD, JAG, DAK, and NAC.

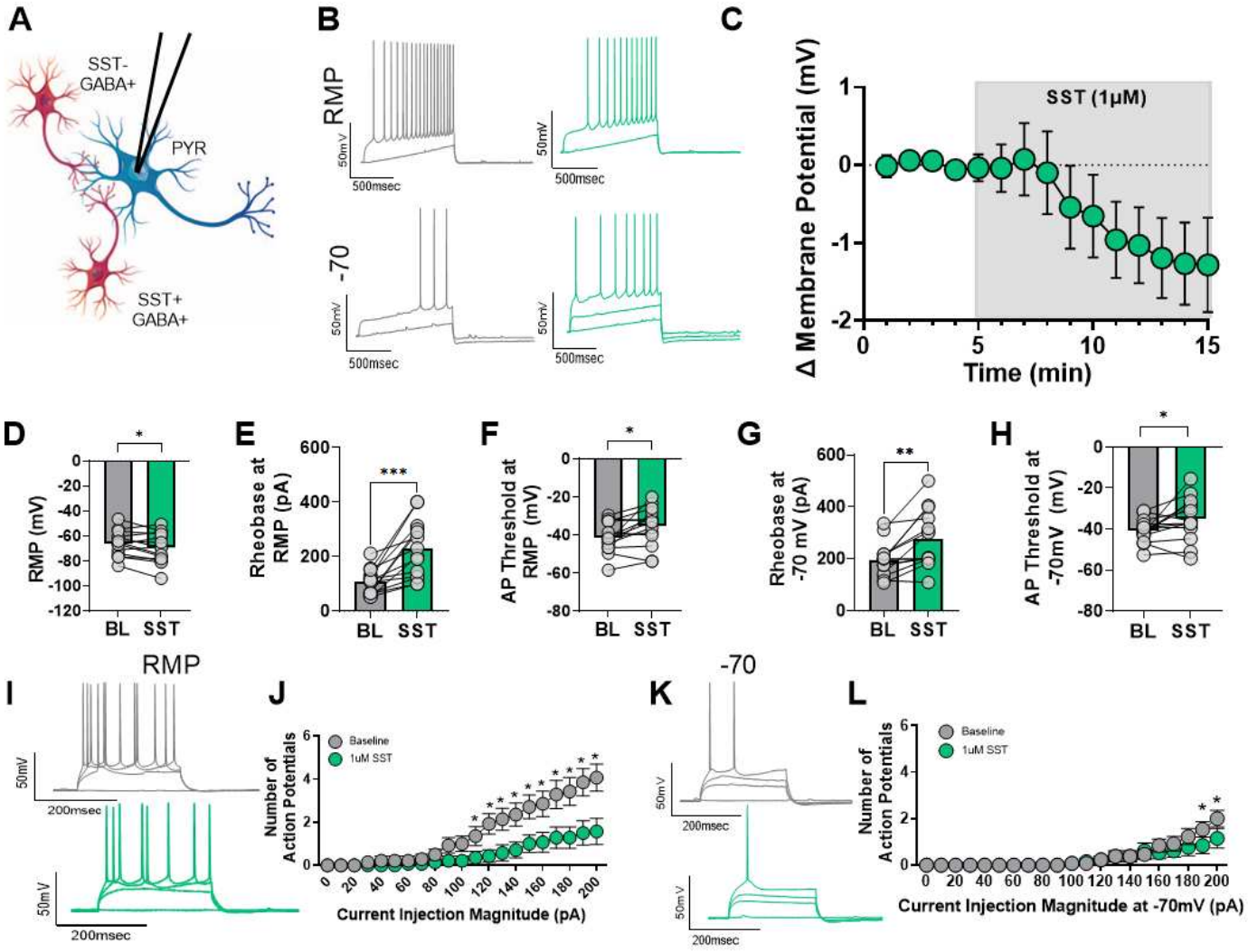

Figure 1 – Somatostatin hyperpolarizes PL pyramidal neurons of female mice.

(A) Schematic of experimental setup. Whole cell current clamp recordings were conducted in PL cortex layer 2/3 pyramidal neurons. **(B)** Representative traces before (grey) and after (green) 1 μM SST application at both RMP (top) and –70 mV (bottom) for rheobase experiments. **(C)** Change in membrane potential over time following SST bath application. **(D)** SST significantly decreased the RMP, **(E)** significantly increased the rheobase at RMP, **(F)** and significantly increased the action potential threshold at RMP**. (G)** Similar effects are seen at the common holding potential of –70 mV, with SST bath application significantly increasing the rheobase, and **(H)** action potential threshold. **(I)** Representative VI traces (corresponding to 0, 110, 150, and 200 pA of current) at RMP before (grey) and after (green) SST application. **(J)** SST significantly reduces the number of

action potentials fired in response to increasing amounts of current injection at RMP. **(K)** Representative VI traces (corresponding to 0, 110, 150, and 200pA of current) at −70 mV before (grey) and after (green) SST application. **(L)** Significant reductions in action potential firing were seen at the highest current injection magnitudes, at the common holding potential of −70 mV. For panels A-J n=14 cells from 12 female mice; for panels K-L n=13 cells from 11 female mice.

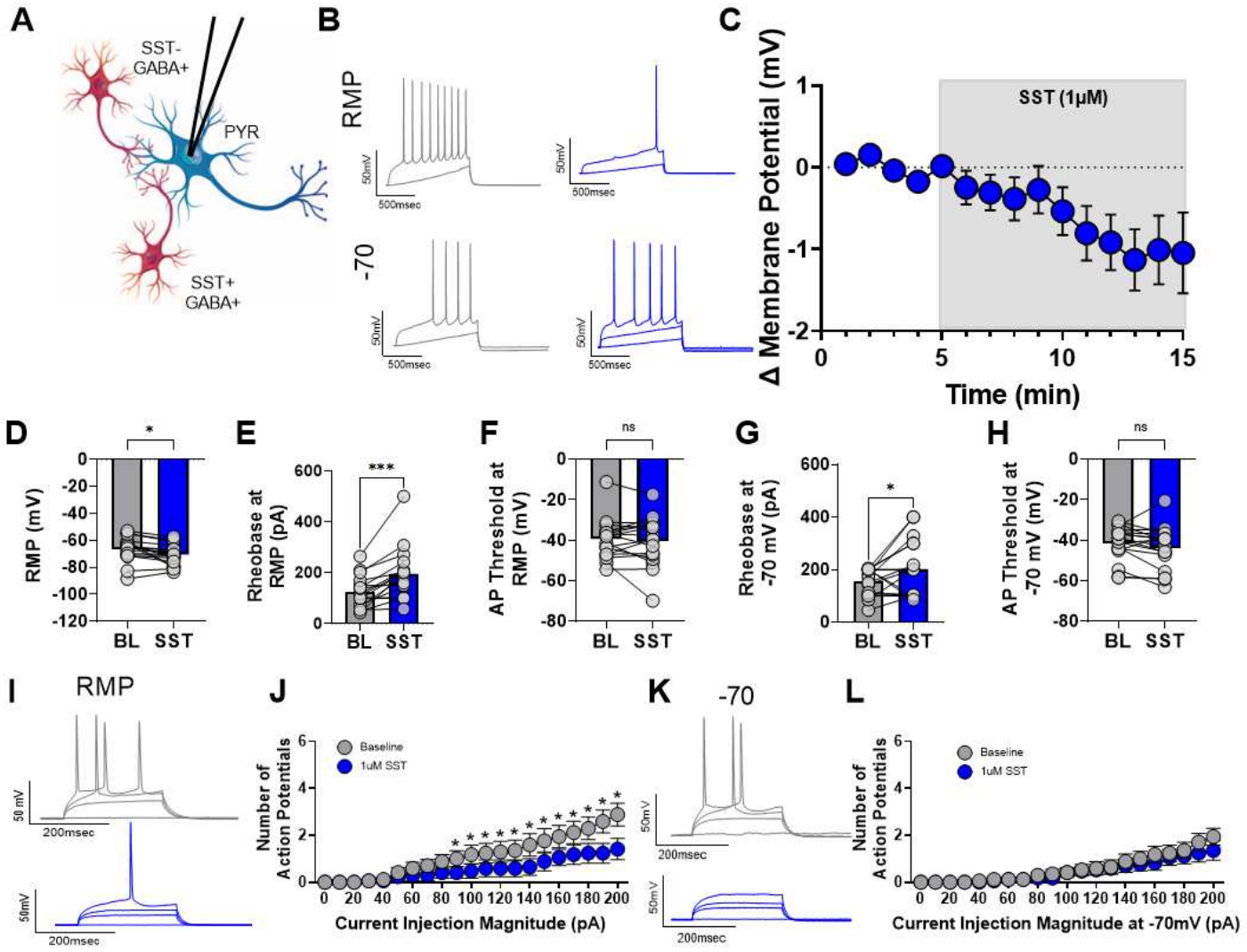

Figure 2 – Somatostatin has a similar hyperpolarizing effect in PL pyramidal neurons of male mice.

(A) Schematic of experimental setup. Whole cell current clamp recording conducted in PL cortex layer 2/3 pyramidal neurons. **(B)** Representative traces before (grey) and after (blue) SST 1 μM application at both RMP and −70 mV for rheobase experiments. **(C)** Change in membrane potential over time following SST bath application**. (D)** SST significantly decreased the RMP **(E)** and rheobase in males. **(F)** The action potential threshold was not changed. **(G)** In addition, the rheobase at −70 mV was significantly increased**, (H)** with no change in the action potential threshold at −70 mV. **(I)** Representative VI traces at RMP (corresponding to 0, 110, 150, and 200 pA of current) before (grey) and after (blue) SST application. **(L)** SST significantly reduces the

number of action potentials fired in response to increasing amounts of current injection at RMP. **(K)** Representative VI traces (corresponding to 0, 110, 150, and 200pA of current) at –70 mV before (grey) and after (blue) SST application. **(L)** No significant change in number of action potentials fired was seen at the common holding potential of –70 mV. For all panels, n= 17 cells from 13 male mice.

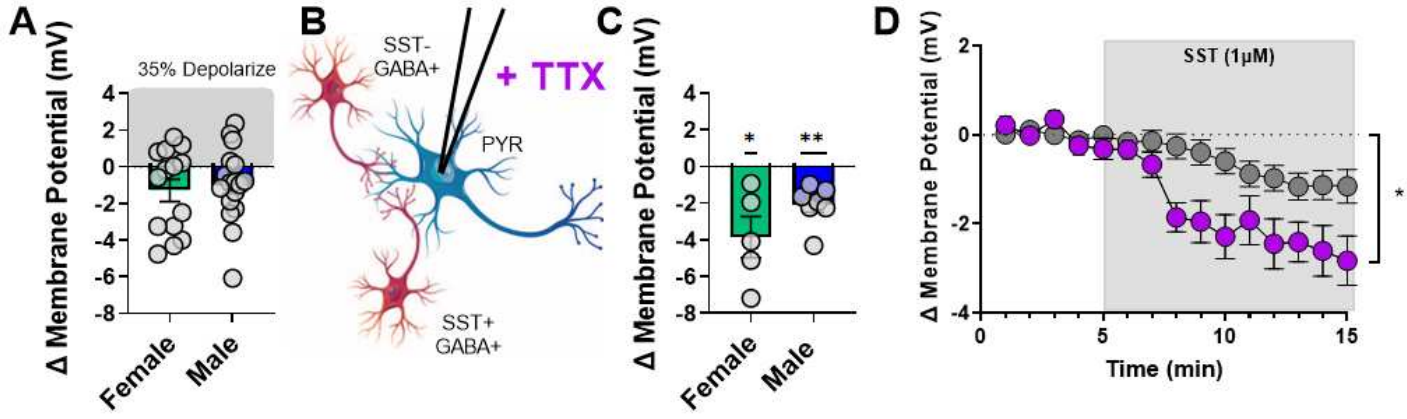

Figure 3 – Somatostatin effects are dependent on PL microcircuit (TTX).

(A) Shift in membrane potential (female in green, male in blue) upon SST administration, reanalyzed from Figures 1-2. 35% of pyramidal neurons depolarize in response to SST. **(B)** Schematic of experimental setup. Whole cell current clamp recordings were conducted in PL cortex layer 2/3 pyramidal neurons with the addition of 500 nM TTX in the aCSF. **(C)** Shift in membrane potential (female in green, male in blue) caused by SST in the presence of TTX. All pyramidal cells hyperpolarize in response to SST when network activity is blocked using TTX, and this effect was significant in both males and females. **(D)** SST significantly hyperpolarizes pyramidal cells (purple, sexes combined; grey, non-TTX data sexes combined from Figure 1C and Figure 2C) following 10 minutes of bath application. Grey bubbles represent non-TTX combined data from figure 1C and figure 2C. For panel A, n= 31 cells from 12 female and 13 male mice, for panels C-D, n= 12 cells from 4 female and 5 male mice.

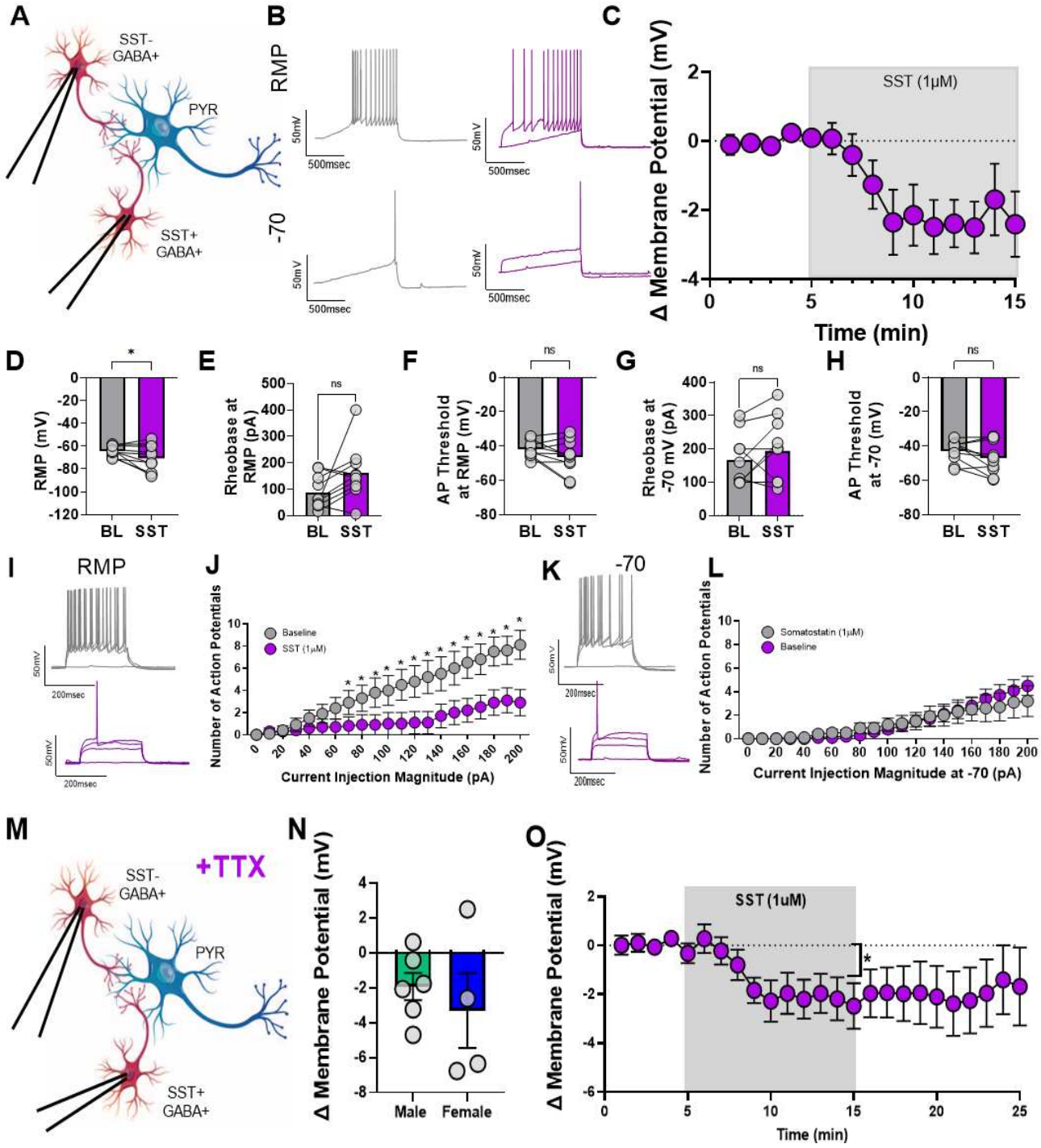

Figure 4 – SST dampens excitability and hyperpolarizes non-pyramidal cells.

(A) Schematic of experimental setup. Whole cell current clamp recordings were conducted in PL cortex layer 2/3 GABA neurons. **(B)** Representative traces before (grey) and after (purple) SST 1 μM application at both RMP (top) and –70 mV (bottom) for rheobase experiments. **(C)** Change in membrane potential over time following

SST bath application**. (D)** SST significantly decreased the RMP. However, **(E)** the rheobase at RMP**,** and **(F)** the action potential threshold at RMP were not significantly changed**. (G)** In addition, the rheobase at –70 mV**,** and **(H)** the action potential threshold at –70 mV were not significantly altered. **(I)** Representative VI traces at RMP (corresponding to 0, 110, 150, 190 pA of injected current) before (grey) and after (purple) SST application. **(J)** SST significantly reduces the number of action potentials fired in response to increasing amounts of current injection at RMP. **(K)** Representative VI traces at –70 mV (corresponding to 0, 110, 150, 190 pA of injected current) before (grey) and after (purple) SST application. **(L)** SST does not significantly alter the number of action potentials fired at the common holding potential of –70 mV. **(M)** Model depicting isolation of network independent effects using TTX while patching PL cortex non-pyramidal neurons. **(N)** Change in membrane potential over time following SST bath application were not significant when sexes were analyzed separately (female in green male in blue). **(O)** Shift in membrane potential following SST bath application was significant when sexes were combined. For panels A-L, n= 10 cells from 2 female and 4 male mice. For panels M-O, n=10 cells from 4 female and 4 male mice.

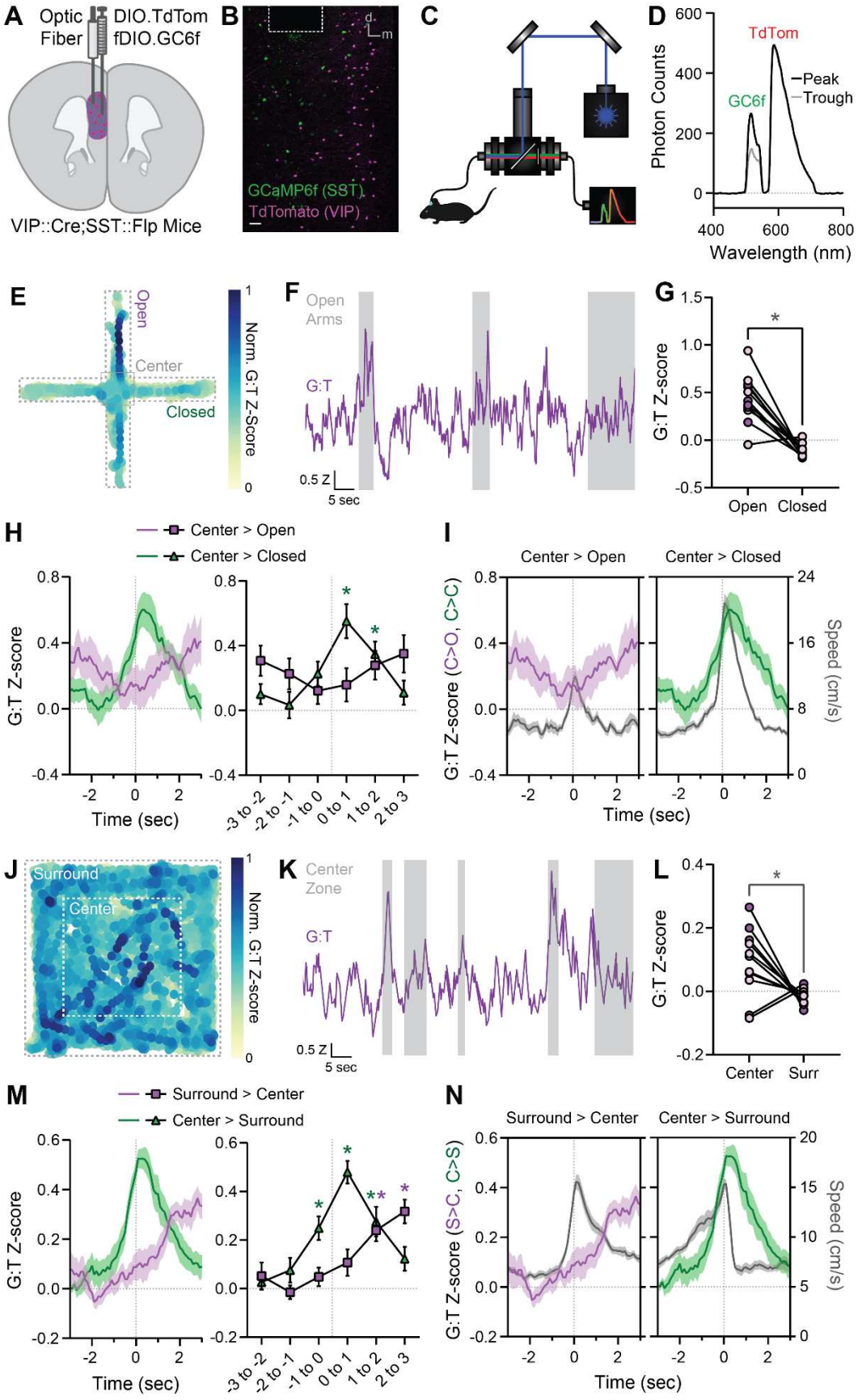

Figure 5 –*In vivo* activity of somatostatin neurons correlates with task-dependent behavior

(A) Schematic of AAV9.CAG.DIO.TdTomato and AAV9.Ef1a.fDIO.GCaMP6f injection with optic fiber implant into unilateral PL cortex of VIP::Cre;SST::Flp mice. **(B)** Sample image of GCaMP6f and TdTomato expression (in putative SST+ and VIP+ interneurons, respectively) and optic fiber placement in PL cortex. Scale bar: 50 μm. **(C)** Schematic of dual-color spectrometer-based in vivo fiber photometry system. **(D)** Sample fluorescence spectrum from PL cortex showing putative GCaMP6f and TdTomato fluorescence at a peak and trough of the GCaMP6f response. **(E)** Sample heatmap of PrL SST+ interneuron Ca2+ dynamics as a function of location in the EPM. Ca2+-dependent GCaMP6f fluorescence intensity is reported as the z-scored ratio of GCaMP6f:TdTomato (G:T) fluorescence, normalized between 0 and 1. **(F)** Sample photometric recording of G:T fluorescence during EPM exploration. Grey bars mark periods of open arm exploration. **(G)** Mean z-scored G:T fluorescence during exploration of the open vs. closed arms of the EPM. Dots represent individual mice (N = 11). Male mice, purple; female mice, pink. **(H)** Z-scored G:T fluorescence aligned to center-to-open arm and center-to-closed arm transitions in the EPM, averaged across mice (N=11, left); 1-sec bins around these transitions (right). **(I)** Z-scored G:T fluorescence and mouse speed aligned to center-to-open arm (left) and center-to-closed arm (right) transitions in the EPM, averaged across mice (N = 11). **(J)** Sample heatmap of z-scored G:T fluorescence (normalized between – and 1) as a function of location in the OF. **(K)** Sample photometric recording of G:T fluorescence during OF exploration. Grey bars mark periods of center zone exploration. **(L)** Mean z-scored G:T fluorescence during exploration of the center and surround of the OF. Dots represent individual mice (N = 11). Male mice, purple; female mice, pink. **(M)** Z-scored G:T fluorescence aligned to surround-to-center zone and center-to-surround zone transitions in the OF, averaged across mice (N=11, left); 1-sec bins around these transitions (right). **(N)** Z-scored G:T fluorescence and mouse speed aligned to surround-to-center zone (left) and center-to-surround zone (right) transitions in the OF, averaged across mice (N=11).

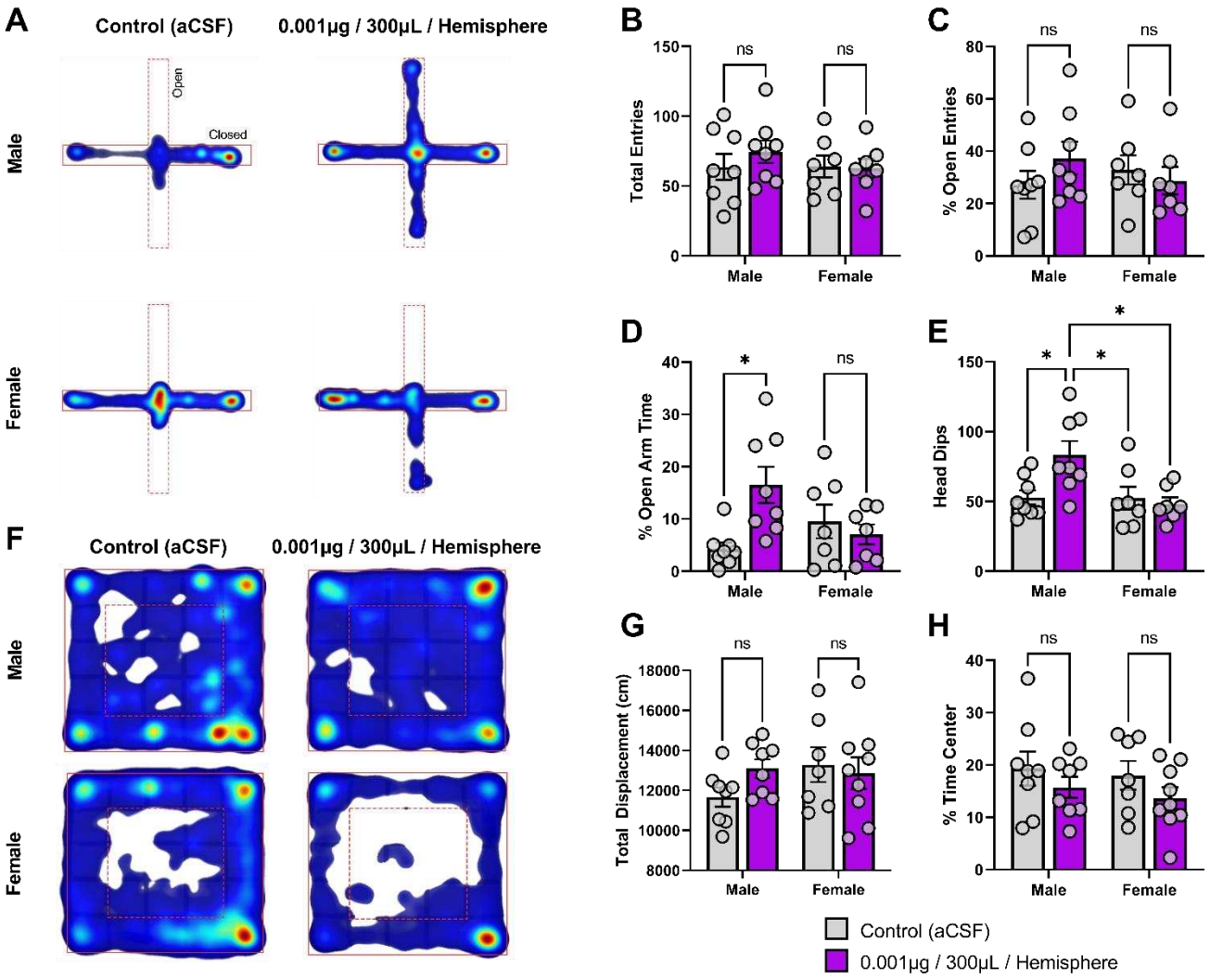

Figure 6 –The SSTR-targeting compound Octreotide decreases avoidance behavior in the EPM

(A) Representative heatmaps of EPM behavior according to mouse location. The open arms are oriented vertically, and closed arms are oriented horizontally for all heatmaps. **(B)** Total entries into both open and closed EPM arms. **(C)** Number of entries into the open arm as a percentage of all entries. **(D)** Percentage time spent in the open arm with respect to total test time. **(E)** Number of head dip extensions outside of the open arm boundaries. **(F)** Representative heatmaps of OFT behavior according to mouse location. **(G)** Total displacement of mice during testing. **(H)** Percentage time spent in the center zone with respect to total test time. For panels A-E n=30 (8 male control, 8 male drug, and 7 female control, 7 female drug) mice for panels F-H n=32(8 male control, 8 male drug and 7 female control, 9 female drug) mice.

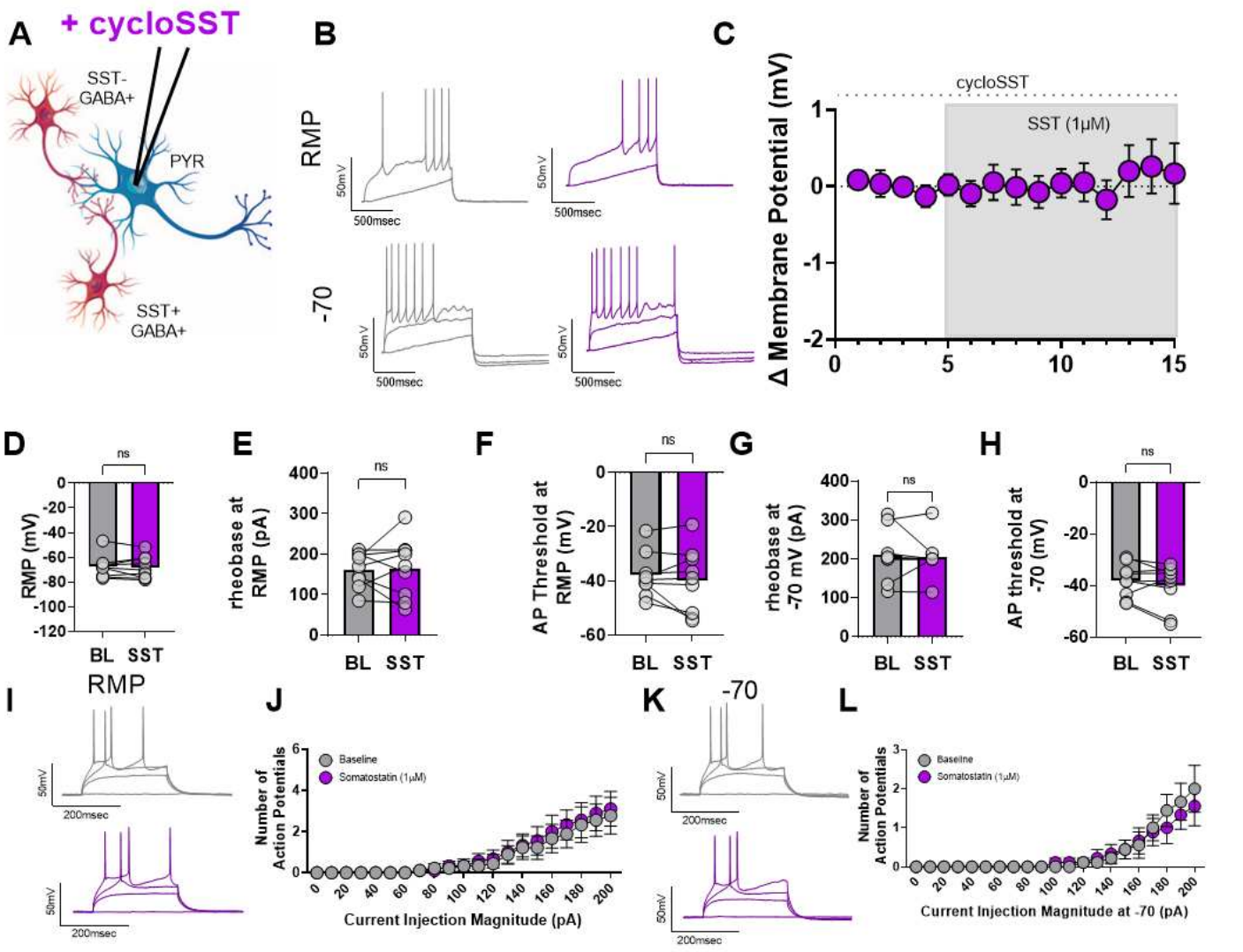

Supplemental Figure 1 – SST-induced alterations in excitability are dependent on SST receptors

(A) Schematic of the experimental setup. Whole cell current clamp recordings were conducted in PL cortex layer 2/3 pyramidal neurons. **(B)** Representative traces before (grey) and after (purple) 1 μM SST bath application with 1 μM cyclo-SST in the aCSF at both RMP and –70 mV for rheobase experiments. **(C)** Change in membrane potential over time following SST bath application with cyclo-SST 1μM in the aCSF. **(D)** SST does not significantly alter the RMP when 1μM cyclo-SST is present ($t_8 = 0.3001$, $p = 0.7717$). **(E)** SST did not significantly change the rheobase at RMP in the presence of 1μM cyclo-SST ($t_8 = 0.1447$, $p = 0.8885$), nor **(F)** the action potential threshold ($t_8 = 0.9659$, $p = 0.3624$). **(G)** The rheobase at –70 mV ($t_8 = 0.3059$, $p = 0.7675$), and **(H)** the action potential threshold at –70 mV ($t_8 = 1.318$, $p = 0.2240$) were not significantly altered. **(I)** Representative

VI traces at RMP (corresponding to 0, 110, 150, and 190 pA of injected current). **(J)** SST does not significantly alter the number of action potentials fired in response to increasing amounts of current injection at RMP in the presence of 1μM cyclo-SST (2-way ANOVA; $F_{current}(20,160) = 9.219$ $p < 0.0001$; $F_{drug}(1,8) = 1.076$ $p = 0.330$; $F_{current\ x\ drug}(20,160) = 0.6466$ $p = 0.8721$). **(K)** Representative VI traces at −70 mV (corresponding to 0, 110, 150, and 190 pA of injected current). **(L)** SST also had no effect on action potential firing at the standard holding potential of −70 mV in the presence of 1 μM cyclo-SST (2-way ANOVA; $F_{current}(20,160) = 10.24$ $p < 0.0001$; $F_{drug}(1,8) = 0.1306$ $p = 0.7272$; $F_{current\ x\ drug}(20,160) = 1.048$ $p = 0.4104$). For all panels, n= 9 cells from 5 female and 3 male mice.

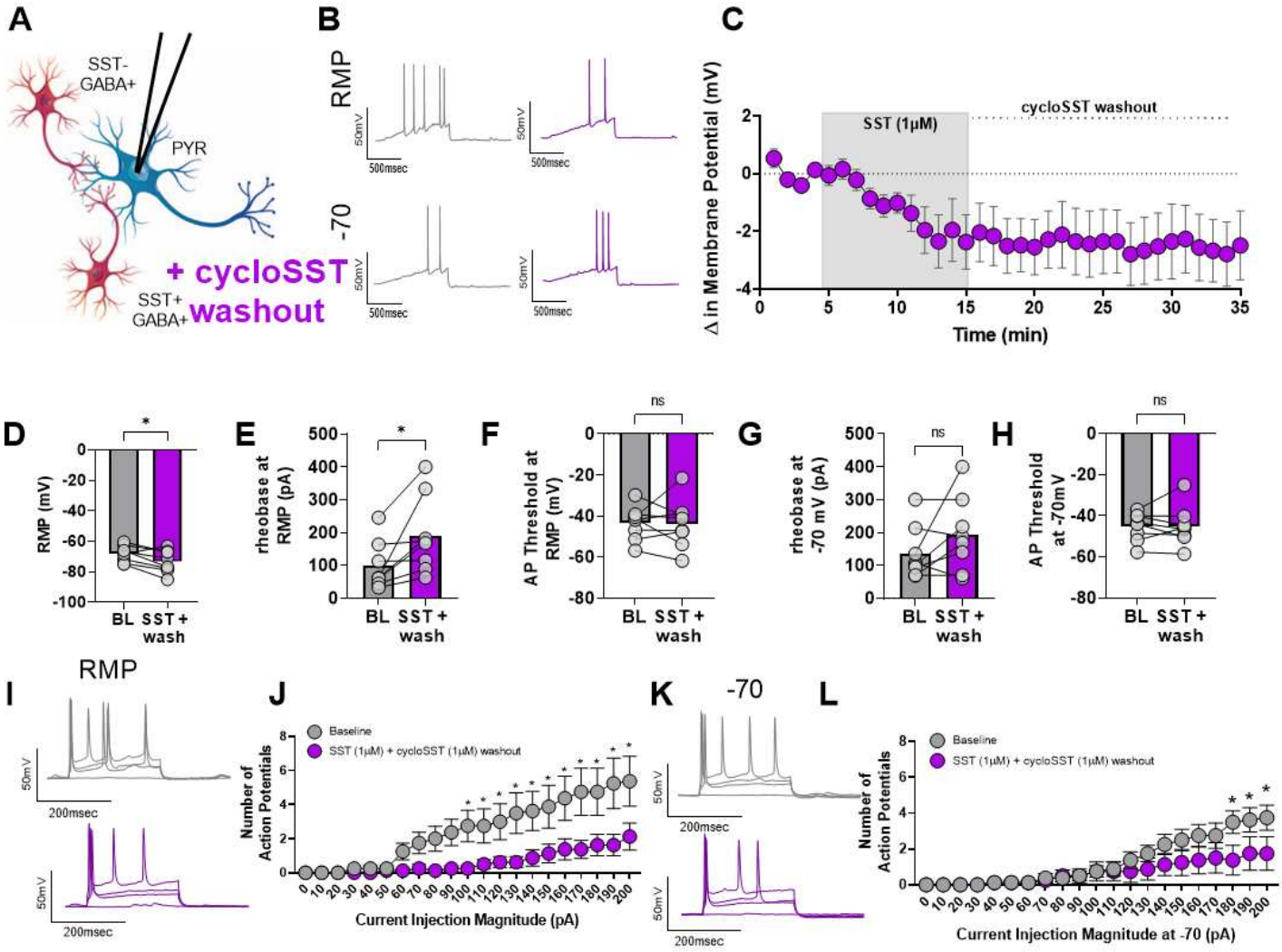

Supplemental Figure 2 – Somatostatin-induced alterations in excitability are insensitive to reversal by SST antagonists

(A) Schematic of experimental setup. Whole cell current clamp recordings were conducted in PL cortex layer 2/3 pyramidal neurons. **(B)** Representative traces before (grey) and after (purple) 1 μM SST followed by a 1 μM cyclo-SST washout at both RMP and –70 mV for rheobase experiments. **(C)** Change in membrane potential over time following SST bath application and cyclo-SST washout. **(D)** SST with cyclo-SST washout significantly reduces the RMP ($t_7 = 2.954$, $p = 0.0213$). **(E)** While the rheobase at RMP was significantly increased by SST and cyclo-SST washout ($t_7 = 2.870$, $p = 0.0240$), **(F)** the action potential threshold was not ($t_7 = 0.1339$, $p = 0.8973$). **(G)** The rheobase at –70 mV ($t_7 = 1.574$, $p = 0.1595$), and **(H)** the action potential threshold at –70 mV ($t_7 =$

0.1218, p = 0.9065) were not significantly altered. **(I)** Representative VI traces at RMP (corresponding to 0, 60, 80, and 140 pA of injected current). **(J)** SST and cyclo-SST washout resulted in a significant interaction between current and SST (2-way ANOVA: $F_{current}(20,140)$ = 16.20 p <0.0001; $F_{drug}(1,7)$ = 4.775 p = 0.0651; $F_{current\ x\ drug}$ (20,140) = 3.170 p <0.0001; significant post-hocs indicated on figure). **(K)** Representative VI traces at –70 mV (corresponding to 0, 60, 80, and 140 pA of injected current). **(L)** Number of action potentials fired remained significant reduced at the holding potential of –70 mV (2-way ANOVA; $F_{current}(20,140)$ = 15.20 p <0.0001; $F_{drug}(1,7)$ = 1.595 p = 0.2471; $F_{current\ x\ drug}$ (20,140) = 2.527 p = 0.0009). For all panels, n= 8 cells from 5 female and 2 male mice.

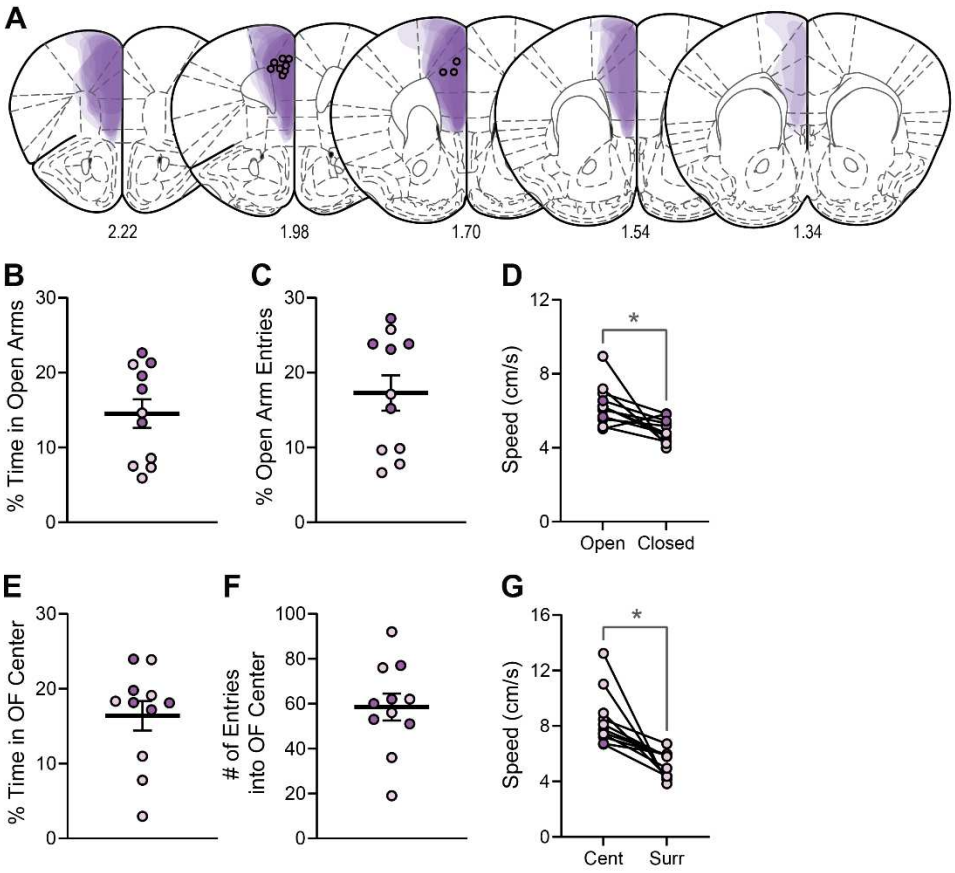

Supplemental Figure 3. Fiber photometry histology and additional EPM and OFT metrics

(A) Combined GCaMP6f and TdTomato expression (purple) and optic fiber placement in PL cortex. Translucent purple areas denote virus expression in individual mice. **(B)** Percent time spent in open arms (open/(open+closed) x 100). **(C)** Percent number of open arm entries (open/(open+closed) x 100). **(D)** Speed (cm/s) of mice when in the open or closed arms (t_{10} = 3.079, p < 0.0117). **(E)** Percent time spent in the center zone of the OFT. **(F)** Number of entries made into the center zone of the OFT. **(G)** Speed (cm/s) of mice when in the center or the surround zones of the OFT (t_{10} = 3.966, p = 0.0027). Male mice, purple; female mice, pink.

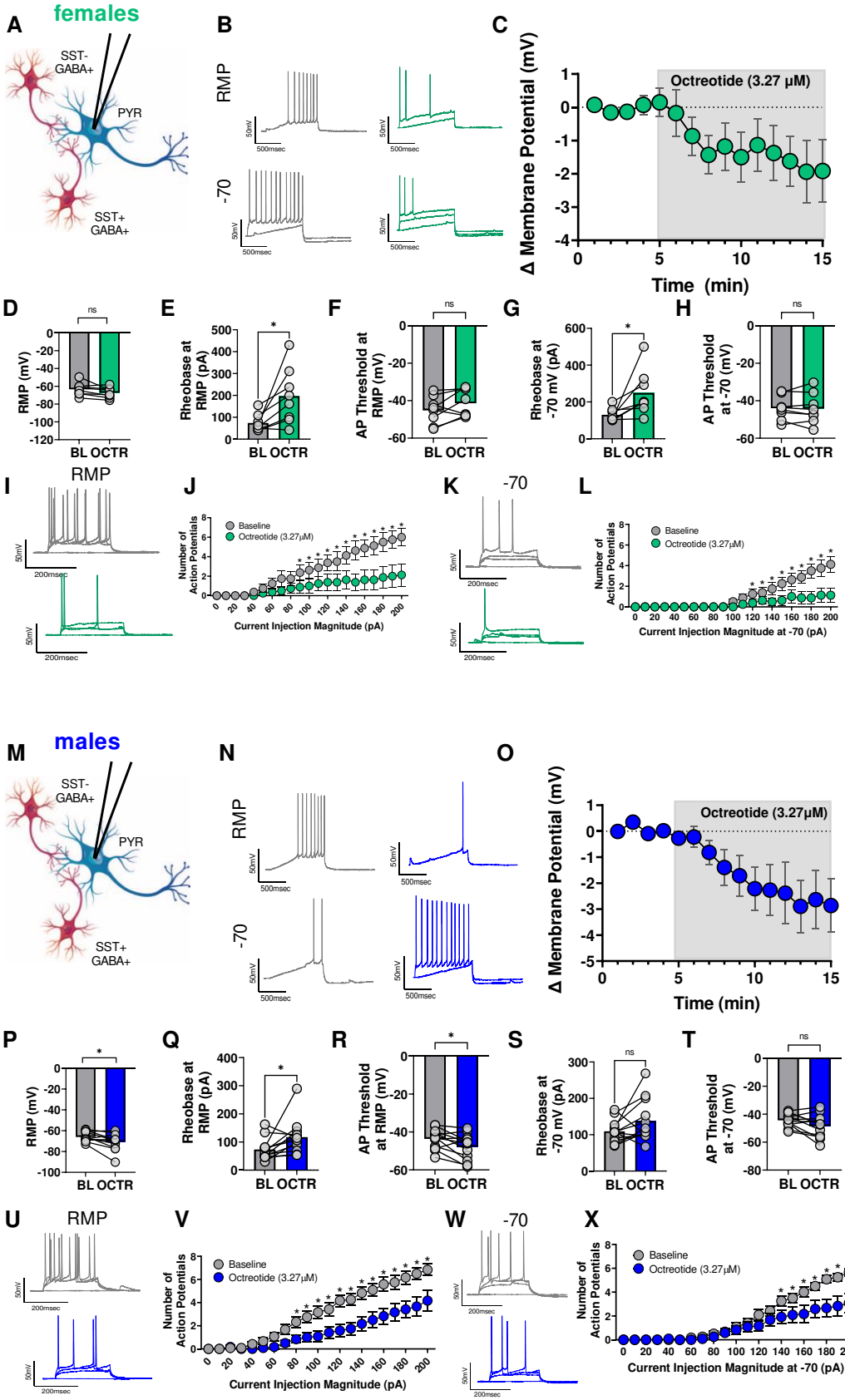

Supplemental Figure 4 – The SST-like agonist Octreotide has similar *ex vivo* effects to SST in both female and male mice.

(A) Schematic of experimental setup. Whole cell current clamp recordings were conducted in PL cortex layer 2/3 pyramidal neurons in females for panels A-L, and in males for panels M-X. **(B)** Representative traces before (grey) and after (green) 1 μM SST application at both RMP and –70 mV for rheobase experiments. **(C)** Change in membrane potential over time following Octreotide bath application**. (D)** Octreotide did not significantly alter membrane potential ($t_7 = 2.239$ $p = 0.0602$). **(E)** The rheobase at RMP was significantly increased ($t_7 = 2.875$, $p = 0.0238$)**,** and **(F)** the action potential threshold was not significantly changed ($t_7 = 1.844$, $p = 0.1077$)**. (G)** In addition, the rheobase at –70 mV was significantly increased ($t_7 = 2.620$, $p = 0.0344$)**,** and **(H)** the action potential threshold at –70 mV was not significantly altered ($t_7 = 0.1792$, $p = 0.8628$)**. (I)** Representative VI traces at RMP (corresponding to 0, 40, 60, 80, 140 pA of injected current) before (grey) and after (green) SST application. **(J)** Octreotide significantly reduces the number of action potentials fired in response to increasing amounts of current injection at RMP (2-way AVNOA; $F_{current}(20,140) = 13.78$; $p < 0.0001$; $F_{drug}(1,7) = 24.19$, $p = 0.0017$; $F_{current\ x\ drug}(20,140) = 11.11$, $p < 0.0001$; significant post-hoc Bonferroni's are indicated on figure). **(K)** Representative VI traces at –70 mV (corresponding to 0, 40, 60, 80, 140 pA of injected current). **(L)** Octreotide significantly reduces the number of action potentials fired at the common holding potential of –70 mV (2-way ANOVA; $F_{current}(20,140) = 10.42$; $p < 0.0001$, $F_{drug}(1,7) = 29.27$, $p = 0.0010$, $F_{current\ x\ drug}(20,140) = 19.18$, $p < 0.0001$**;** significant post-hoc Bonferroni's are indicated on figure). **(M)** Schematic of experimental setup. Whole cell current clamp recordings were conducted in PL cortex layer 2/3 pyramidal neurons in males for panels M-X. **(N)** Representative traces before (grey) and after (blue) SST 1 μM application at both RMP and –70 mV for rheobase experiments. **(O)** Change in membrane potential over time following Octreotide bath application. **(P)** Octreotide significantly reduced the RMP in males ($t_{11} = 2.738$ $p = 0.0193$). **(Q)** The rheobase at RMP was significantly increased ($t_{11} = 2.341$ $p = 0.0391$)**,** and **(R)** the action potential threshold was significantly reduced ($t_{11} = 2.848$ $p = 0.0159$)**. (S)** In addition, the rheobase at –70 mV was not significantly altered ($t_{11} = 1.745$ $p = 0.1088$)**, (T)** while the action potential threshold at –70 mV was not significantly altered ($t_{11} = 2.200$ $p = 0.0501$)**. (U)** Representative VI traces at RMP (corresponding to 0, 40, 60, 80, 140 pA of injected current) before (grey) and after (green) SST application. **(V)** Octreotide significantly reduces the number of action potentials fired in

response to increasing amounts of current injection at RMP (2-way ANOVA; $F_{current}(20,220) = 75.68$; $p < 0.0001$; $F_{drug}(1,11) = 11.53$, $p = 0.0060$; $F_{current\ x\ drug}(20,220) = 5.769$, $p < 0.0001$; significant post-hoc Bonferroni's are indicated on figures). **(W)** Representative VI traces at −70 mV (corresponding to 0, 40, 60, 80, 140 pA of injected current). **(X)** Octreotide significantly reduces the number of action potentials fired at the common holding potential of −70 mV (2-way ANOVA; $F_{current}(20,220) = 53.05$ $p < 0.0001$; $F_{drug}(1,11) = 5.129$ $p = 0.0447$; $F_{current\ x\ drug}(20,220) = 6.954$ $p < 0.0001$; **X**, significant post-hoc Bonferroni's are indicated on figures). For panels A-L n = 8 cells from 5 female mice. For panels M-X n = 12 cells from 9 male mice.

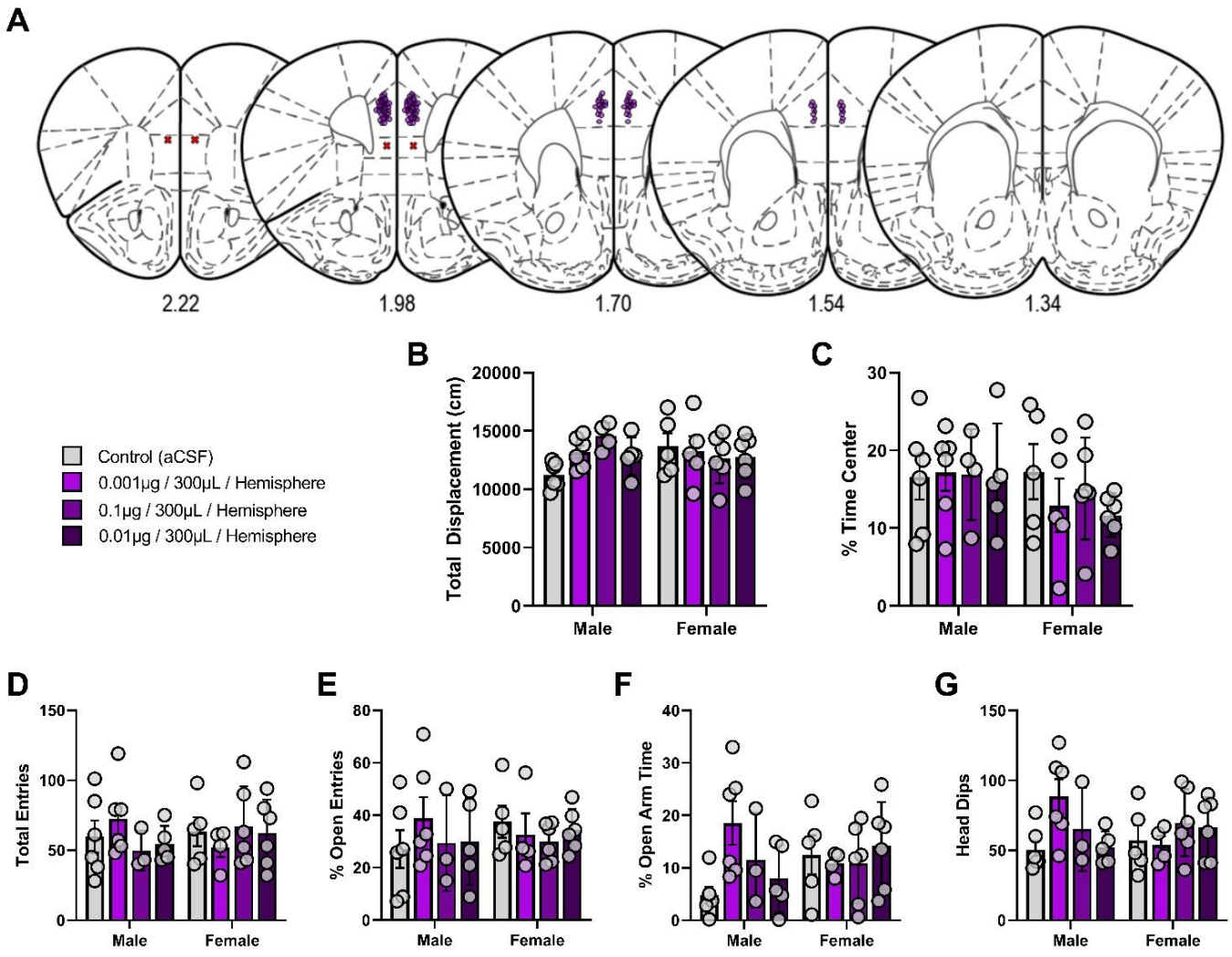

Supplemental Figure 5 – Pilot dose response curves for bilateral administration of Octreotide to the PL cortex

(A) Histological verification of cannula placement. 2 out of 70 mice were removed for missed cannula placement. **(B)** Octreotide does not significantly alter the total displacement in the OFT (2-way ANOVA; $F_{sex}(1,35)$ = 0.06172, $p=0.8053$; $F_{drug}(3,35)$ = 0.7235, p = 0.5448, $F_{sex\ x\ drug}(3,35)$ = 2.255, p =0.0992; significant post-hoc Tukey's are indicated on figure). **(C)** Octreotide does not significantly alter % time in the center of the OFT (2-way ANOVA; $F_{sex}(1,35)$ = 1.504, $p=0.2282$; $F_{drug}(3,35)$ = 0.4154, p = 0.7430, $F_{sex\ x\ drug}(3,35)$ = 0.3811, p =0.7672; significant post-hoc Tukey's are indicated on figure). **(D)** Octreotide does not significantly alter number of total entries into the open and closed arms (2-way ANOVA; $F_{sex}(1,33)$ = 0.07206, $p=0.7900$; $F_{drug}(3,33)$ = 0.07471, p = 0.9732, $F_{sex\ x\ drug}(3,33)$ = 1.067, p =0.3763; significant post-hoc Tukey's are indicated on figure). **(E)** In a pilot

cohort of mice, Octreotide did not significantly alter percent open arm entries as a percentage of total entries in the EPM (2-way ANOVA; $F_{sex}(1, 33) = 0.2223$, $p=0.6404$; $F_{drug}(3,33) = 0.2552$, $p = 0.8571$, $F_{sex\ x\ drug}(3,33) = 0.5567$, $p = 0.6473$; significant post-hoc Tukey's are indicated on figure). **(F)** Octreotide does not significantly alter % time in the open arm (2-way ANOVA; $F_{sex}(1,33) = 0.3389$, $p=0.5644$; $F_{drug}(3,33) = 1.126$, $p = 0.3527$, $F_{sex\ x\ drug}(3,33) = 2.226$, $p = 0.1036$; significant post-hoc Tukey's are indicated on figure). **(G)** Octreotide does not significantly alter number of head dips off the open arm (2-way ANOVA; $F_{sex}(1,33) = 0.09816$, $p=0.7560$; $F_{drug}(3,33) = 1.252$, $p = 0.3066$, $F_{sex\ x\ drug}(3,33) = 2.470$, $p = 0.0791$; significant post-hoc Tukey's are indicated on figure). Based on pilot data, subsequent experiments were conducted with the lowest dose, which most closely approximated those used for electrophysiology experiments.

REFERENCES

Abbas, A. I. *et al.* (2018) 'Somatostatin Interneurons Facilitate Hippocampal-Prefrontal Synchrony and Prefrontal Spatial Encoding', *Neuron*, 100, pp. 926–939. doi: 10.1016/j.neuron.2018.09.029.

Adhikari, A., Topiwala, M. A. and Gordon, J. A. (2010) 'Synchronized activity between the ventral hippocampus and the medial prefrontal cortex during anxiety', *Neuron*, 65(2), pp. 257–269. doi: 10.1016/J.NEURON.2009.12.002.

Adhikari, A., Topiwala, M. A. and Gordon, J. A. (2011) 'Single units in the medial prefrontal cortex with anxiety-related firing patterns are preferentially influenced by ventral hippocampal activity', *Neuron*, 71(5), pp. 898–910. doi: 10.1016/J.NEURON.2011.07.027.

Brockway, D. F. and Crowley, N. A. (2020) 'Turning the ′Tides on Neuropsychiatric Diseases: The Role of Peptides in the Prefrontal Cortex', *Frontiers in Behavioral Neuroscience*, 14. doi: 10.3389/fnbeh.2020.588400.

Crowley, N. A. *et al.* (2016) 'Dynorphin Controls the Gain of an Amygdalar Anxiety Circuit', *Cell Reports*, 14(12), pp. 2774–2783. doi: 10.1016/j.celrep.2016.02.069.

Crowley, N. A. and Joffe, M. E. (2021) 'Developing breakthrough psychiatric treatments by modulating G protein-coupled receptors on prefrontal cortex somatostatin interneurons', *Neuropsychopharmacology : official publication of the American College of Neuropsychopharmacology*. doi: 10.1038/S41386-021-01119-X.

Cummings, K. A. and Clem, R. L. (2020) 'Prefrontal somatostatin interneurons encode fear memory', *Nature Neuroscience*, 23(1), pp. 61–74. doi: 10.1038/s41593-019-0552-7.

Dao, N. C. *et al.* (2020) 'Forced Abstinence From Alcohol Induces Sex-Specific Depression-Like Behavioral and Neural Adaptations in Somatostatin Neurons in Cortical and Amygdalar Regions', *Frontiers in Behavioral Neuroscience*, 14. doi: 10.3389/fnbeh.2020.00086.

Dao, N. C. *et al.* (2021) 'Somatostatin neurons control an alcohol binge drinking prelimbic microcircuit in mice', *Neuropsychopharmacology 2021*, pp. 1–12. doi: 10.1038/s41386-021-01050-1.

Dao, N. C., Brockway, D. F. and Crowley, N. A. (2019) 'In Vitro Optogenetic Characterization of Neuropeptide Release from Prefrontal Cortical Somatostatin Neurons', *Neuroscience*, 419, pp. 1–4. doi: 10.1016/j.neuroscience.2019.08.014.

Delfs, J. R. and Dichter, M. A. (1983) 'Effects of somatostatin on mammalian cortical neurons in culture: Physiological actions and unusual dose response characteristics', *Journal of Neuroscience*, 3(6), pp. 1176–1178. doi: 10.1523/jneurosci.03-06-01176.1983.

Engin, E. *et al.* (2008) 'Anxiolytic and antidepressant effects of intracerebroventricularly administered somatostatin: Behavioral and neurophysiological evidence', *Neuroscience*, 157(3), pp. 666–676. doi: 10.1016/J.NEUROSCIENCE.2008.09.037.

Engin, E. and Treit, D. (2009) 'Anxiolytic and antidepressant actions of somatostatin: The role of sst2 and sst3 receptors', *Psychopharmacology*, 206(2), pp. 281–289. doi: 10.1007/S00213-009-1605-5/FIGURES/2.

Fung, S. J. *et al.* (2014) 'Schizophrenia and bipolar disorder show both common and distinct changes in cortical interneuron markers', *Schizophrenia Research*, 155(1–3), pp. 26–30. doi: 10.1016/j.schres.2014.02.021.

Girgenti, M. J. *et al.* (2019) 'Prefrontal cortex interneurons display dynamic sex-specific stress-induced transcriptomes', *Translational Psychiatry*, 9(1). doi: 10.1038/s41398-019-0642-z.

Hashimoto, T. *et al.* (2008) 'Conserved regional patterns of GABA-related transcript expression in the neocortex of subjects with schizophrenia', *American Journal of Psychiatry*, 165(4), pp. 479–489. doi: 10.1176/appi.ajp.2007.07081223.

Joffe, M. E. *et al.* (2022) 'Acute restraint stress redirects prefrontal cortex circuit function through mGlu 5 receptor plasticity on somatostatin-expressing interneurons', *Neuron*, 110(6), pp. 1068-1083.e5. doi: 10.1016/J.NEURON.2021.12.027.

Kane, G. A. *et al.* (2020) 'Real-time, low-latency closed-loop feedback using markerless posture tracking', *eLife*, 9, pp. 1–29. doi: 10.7554/ELIFE.61909.

Kash, T. L. *et al.* (2015) 'Neuropeptide regulation of signaling and behavior in the BNST', *Molecules and Cells*. Korean Society for Molecular and Cellular Biology, pp. 1–13. doi: 10.14348/molcells.2015.2261.

Lee, A. T. *et al.* (2019) 'VIP Interneurons Contribute to Avoidance Behavior by Regulating Information Flow across Hippocampal-Prefrontal Networks Article VIP Interneurons Contribute to Avoidance Behavior by Regulating Information Flow across Hippocampal-Prefrontal Networks', *Neuron*, 102, pp. 1223–1234. doi: 10.1016/j.neuron.2019.04.001.

Leresche, N. *et al.* (2000) 'Somatostatin inhibits GABAergic transmission in the sensory thalamus via presynaptic receptors', *Neuroscience*, 98(3), pp. 513–522. doi: 10.1016/S0306-4522(00)00107-X.

Liguz-Lecznar, M., Urban-Ciecko, J. and Kossut, M. (2016) 'Somatostatin and somatostatin-containing neurons in shaping neuronal activity and plasticity', *Frontiers in Neural Circuits*. Frontiers Media S.A. doi: 10.3389/fncir.2016.00048.

Lopes, G. *et al.* (2015) 'Bonsai: An event-based framework for processing and controlling data streams', *Frontiers in Neuroinformatics*, 9(APR), p. 7. doi: 10.3389/FNINF.2015.00007/ABSTRACT.

Lopez-Huerta, V. G. *et al.* (2008) 'Presynaptic modulation by somatostatin in the neostriatum', *Neurochemical research*, 33(8), pp. 1452–1458. doi: 10.1007/S11064-007-9579-3.

Lowery-Gionta, E. G. *et al.* (2018) 'Chronic stress dysregulates amygdalar output to the prefrontal cortex', *Neuropharmacology*, 139, pp. 68–75. doi: 10.1016/J.NEUROPHARM.2018.06.032.

Mathis, A. *et al.* (2018) 'DeepLabCut: markerless pose estimation of user-defined body parts with deep learning', *Nature Neuroscience 2018 21:9*, 21(9), pp. 1281–1289. doi: 10.1038/s41593-018-0209-y.

Merighi, A. (2018) 'Costorage of high molecular weight neurotransmitters in large dense core vesicles of mammalian neurons', *Frontiers in Cellular Neuroscience*, 12, p. 272. doi: 10.3389/FNCEL.2018.00272/BIBTEX.

Momiyama, T. and Zaborszky, L. (2006) 'Somatostatin presynaptically inhibits both GABA and glutamate release onto rat basal forebrain cholinergic neurons', *Journal of Neurophysiology*, 96(2), pp. 686–694. doi: 10.1152/jn.00507.2005.

Ochi, R. *et al.* (2022) 'Patterns of functional connectivity alterations induced by alcohol reflect somatostatin interneuron expression in the human cerebral cortex', *Scientific Reports 2022 12:1*, 12(1), pp. 1–9. doi: 10.1038/s41598-022-12035-5.

Padilla-Coreano, N. *et al.* (2016) 'Direct Ventral Hippocampal-Prefrontal Input Is Required for Anxiety-Related Neural Activity and Behavior', *Neuron*, 89(4), pp. 857–866. doi: 10.1016/J.NEURON.2016.01.011.

Padilla-Coreano, N. *et al.* (2019) 'Hippocampal-Prefrontal Theta Transmission Regulates Avoidance Behavior', *Neuron*, 104, pp. 601-610.e4. doi: 10.1016/j.neuron.2019.08.006.

Patel, Y. C. *et al.* (1994) 'All five cloned human somatostatin receptors (hSSTR1-5) are functionally coupled to

adenylyl cyclase', *Biochemical and Biophysical Research Communications*, 198(2), pp. 605–612. doi: 10.1006/bbrc.1994.1088.

Pichler, R. *et al.* (2002) 'Letter to the Editor Is there a gender difference of somatostatin-receptor density in the human brain?', *Neuroendocrinology Letters*, 23(6), pp. 235602–235604. Available at: www.nel.edu (Accessed: 15 June 2022).

Pittman, Q. J. and Siggins, G. R. (1981) 'Somatostatin hyperpolarizes hippocampal pyramidal cells in vitro', *Brain Research*, 221(2), pp. 402–408. doi: 10.1016/0006-8993(81)90791-5.

van den Pol, A. N. (2012) 'Neuropeptide Transmission in Brain Circuits', *Neuron*. NIH Public Access, pp. 98–115. doi: 10.1016/j.neuron.2012.09.014.

Riedemann, T. and Sutor, B. (2019) 'Long-lasting actions of somatostatin on pyramidal cell excitability in the mouse cingulate cortex', *Neuroscience Letters*, 698, pp. 217–223. doi: 10.1016/J.NEULET.2019.01.034.

Robinson, S. L. and Thiele, T. E. (2020) 'A role for the neuropeptide somatostatin in the neurobiology of behaviors associated with substances abuse and affective disorders', *Neuropharmacology*. Elsevier Ltd, p. 107983. doi: 10.1016/j.neuropharm.2020.107983.

Sajadi, A. *et al.* (2016) 'Neurodegeneration in an Animal Model of Chronic Amyloid-beta Oligomer Infusion Is Counteracted by Antibody Treatment Infused with Osmotic Pumps', *Journal of Visualized Experiments : JoVE*, 2016(114). doi: 10.3791/54215.

Schreff, M. *et al.* (2000) 'Distribution, Targeting, and Internalization of the sst4 Somatostatin Receptor in Rat Brain', *The Journal of Neuroscience*, 20(10), p. 3785. doi: 10.1523/JNEUROSCI.20-10-03785.2000.

Selmer, I. S. *et al.* (2000) 'Advances in understanding neuronal somatostatin receptors', *Regulatory Peptides*, 90(1–3), pp. 1–18. doi: 10.1016/S0167-0115(00)00108-7.

Sibille, E. *et al.* (2011) 'GABA-related transcripts in the dorsolateral prefrontal cortex in mood disorders', *International Journal of Neuropsychopharmacology*, 14(6), pp. 721–734. doi: 10.1017/S1461145710001616.

Song, Y.-H., Yoon, J. and Lee, S.-H. (2021) 'The role of neuropeptide somatostatin in the brain and its application in treating neurological disorders', *Experimental & Molecular Medicine*, 53, pp. 328–338. doi: 10.1038/s12276-021-00580-4.

Stark, K. L. *et al.* (2008) 'Altered brain microRNA biogenesis contributes to phenotypic deficits in a 22q11-

deletion mouse model', *Nature genetics*, 40(6), pp. 751–760. doi: 10.1038/NG.138.

Ting, J. T. *et al.* (2018) 'Preparation of Acute Brain Slices Using an Optimized N-Methyl-D-glucamine Protective Recovery Method', *Journal of visualized experiments : JoVE*, (132). doi: 10.3791/53825.

Urban-Ciecko, J. and Barth, A. L. (2016) 'Somatostatin-expressing neurons in cortical networks', *Nature Reviews Neuroscience*, 17(7), pp. 401–409. doi: 10.1038/nrn.2016.53.

Wang, H. *et al.* (2022) 'A toolkit of highly selective and sensitive genetically encoded neuropeptide sensors', *bioRxiv*, p. 2022.03.26.485911. doi: 10.1101/2022.03.26.485911.

Xiong, H. *et al.* (2021) 'Probing neuropeptide volume transmission in vivo by a novel all-optical approach', *bioRxiv*, p. 2021.09.10.459853. doi: 10.1101/2021.09.10.459853.

Yeung, M. and Treit, D. (2012) 'The anxiolytic effects of somatostatin following intra-septal and intra-amygdalar microinfusions are reversed by the selective sst2 antagonist PRL2903', *Pharmacology Biochemistry and Behavior*, 101(1), pp. 88–92. doi: 10.1016/J.PBB.2011.12.012.